

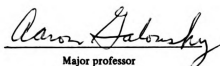


This is to certify that the
thesis entitled
NEUTRON/GAMMA-RAY PULSE SHAPE DISCRIMINATION
IN LIQUID ORGANIC SCINTILLATORS
presented by

John Edward Yurkon

has been accepted towards fulfillment
of the requirements for

M.S. degree in Physics


Major professor

Date Nov. 8/1979



OVERDUE FINES:

25¢ per day per item

RETURNING LIBRARY MATERIALS:

Place in book return to remove
charge from circulation records

|

|

NEUTRON/GAMMA-RAY PULSE SHAPE DISCRIMINATION
IN LIQUID ORGANIC SCINTILLATORS

By

John Edward Yurkon

A THESIS

Submitted to
Michigan State University
in partial fulfillment of the requirements
for the degree of

MASTER OF SCIENCE

Department of Physics

ABSTRACT

NEUTRON/GAMMA-RAY PULSE SHAPE DISCRIMINATION IN LIQUID ORGANIC SCINTILLATORS

By

John Edward Yurkon

Origins of pulse shape differences are discussed. A method of using these differences for neutron/gamma-ray discrimination is also discussed and the factors affecting the qualities of the pulse shape discrimination are shown on theoretical grounds and then measured.

Optimal pulse shape discrimination is measured for the liquid organic scintillators NE213 and NE224.

Problems with a large volume neutron time-of-flight detector at Michigan State University are presented along with suggested solutions.

ACKNOWLEDGMENTS

I would like to thank Dr. A. Galonsky for his careful reading of this thesis and for his guidance and help in re-searching the material, and in performing the associated experiments.

The assistance of Mr. M. Wallace was very helpful in preparing the figures in this thesis. Also the patient explanations of the use of the computer facilities by Mr. R. Melin and Mr. R. Fox were helpful in the preparation of this thesis. The glass-blowing shop of the Department of Chemistry constructed the various cells used in researching this thesis. I would like to thank Ms. D. Barrett for her help in organizing the material used in preparation of this thesis and for her encouragement to stick with it.

The typing of this thesis by Mrs. Betty McClure is greatly appreciated.

Finally, I would like to thank my parents and friends for their support during my graduate study.

TABLE OF CONTENTS

	Page
LIST OF TABLES	iii
LIST OF FIGURES	iv
1. INTRODUCTION	1
2. THEORY OF PULSE SHAPE DISCRIMINATION	2
2.1 Excitation Process and Decay	2
2.2 Zero-Crossover Technique	6
2.3 Model of System Performance	10
2.4 Calculation of System Performance	15
3. FIGURE OF MERIT FOR NE213 AND NE224 UNDER IDEAL CONDITIONS	22
3.1 Figure of Merit for NE213	22
3.2 Figure of Merit for NE224	33
4. LIGHT COLLECTION IN THE SCINTILLATION COUNTER	36
4.1 Effects of Light Attenuation on Figure of Merit	36
4.2 Light Collection Problems with a Large Neutron Time-of-Flight Detector at Michigan State University	36
5. DEOXYGENATION OF SCINTILLATION COUNTERS	45
5.1 Method of Deoxygenation	45
5.2 Diffusion Model	45
6. A NEUTRON TIME-OF-FLIGHT DETECTOR WITH IMPROVED PULSE SHAPE DISCRIMINATION	50
6.1 The Detector	50
6.2 Performance	51
6.2.1 Detector filled with NE213	51
6.2.2 Detector filled with NE224	56
6.3 Comments	56

	Page
7. PHOTOMULTIPLIER PROBLEMS	62
7.1 Gas Ionization	62
7.2 After-Pulses in the Present System	62
8. CONCLUSION	68
APPENDIX A - COMPUTER PROGRAM FOR CALCULATING $\bar{\epsilon}$, D and ϵ	70
APPENDIX B - COMPUTER PROGRAM FOR GENERATING PULSE SHAPE SIGNATURES	72
APPENDIX C - COMPUTER PROGRAM FOR CALCULATING FIGURE OF MERIT D AS A FUNCTION OF PULSE HEIGHT FRACTION K	74
APPENDIX D - COMPUTER PROGRAM FOR CALCULATION LIGHT ATTENUATION IN A RECTANGULAR DETECTOR	76
APPENDIX E - LIGHT ATTENUATION IN LIQUID ORGANIC SCINTILLATORS	79
LIST OF REFERENCES	100

LIST OF TABLES

Table	Page
1. Data for Decay Times and Relative Contributions of Decay Modes in NE213. Data taken from Sabbah and Suhami ¹³	17
2. Theoretical Figure of Merit (D) for a Given Number of Photoelectrons (P)	19
3. Data for Number of Photoelectrons per KeV for an NE213 Scintillator Mounted on an RCA 8850 Photo-multiplier	28
4. Theoretical Figure of Merit (M) at a Given Energy for NE213	29
5. Figure of Merit (M) for a 45 mm x 50 mm NE213 Scintillator	32
6. Figure of Merit (M) for a 45 mm x 50 mm NE224 Scintillator	35
7. Theoretical Light Transmission, in Percent, through a Rectangular Scintillator of Dimensions 2.7 cm x 12.8 cm x 83.8 cm. The Source Positions X, Y, and Z are Defined in Figure 13.	40
8. Figure of Merit (M) for a 1.24 m x 45 mm NE213 Scintillator with Source at Near End of Scintillator	52
9. Figure of Merit (M) for a 1.24 m x 45 mm NE213 Scintillator with Source at Center of Scintillator	54
10. Figure of Merit for a 1.24 m x 45 mm NE224 Scintillator with Source at Near End of Scintillator	58
11. Figure of Merit for a 1.24 m x 45 mm NE224 Scintillator with Source at Center of Scintillator	60
E1. Attenuation Lengths in Meters as Measured with Laser Light	85
E2. Wavelength-Averaged Attenuation Length in Meters for Unpainted Cells Containing NE213	93
E3. Practical Attenuation Lengths in Meters for Black-Painted Cells containing NE213	95

LIST OF FIGURES

Figure	Page
1. Energy transfer process from solvent to solute.	4
2. Production of T_1 states. The arrow represents the spin of the electron.	5
3. Block diagram of pulse shape discrimination electronics.	7
4. Unipolar and bipolar pulse shaping.	9
5. RC shaping circuit for dynode pulse.	11
6. Plots of expected PSD signatures for NE213.	20
7. Figure of merit versus discrimination level.	21
8. Scintillator cell, 50 mm x 45 mm.	23
9. Schematic of LED pulser of Hagen and Eklund. ¹⁹	25
10. Electronics for determining P_{e1} .	26
11. NE213 PSD spectra 45 mm x 50 mm cell.	31
12. NE224 PSD spectra 45 mm x 50 mm cell.	34
13. A large neutron time-of-flight detector.	37
14. Placement of scintillation cell.	41
15. Electronics for measuring light pipe attenuation.	42
16. Compton edge spectra without light pipe (a) and with light pipe (b).	43
17. PSD for NE213 cell 1.24 m, near end.	53
18. PSD for NE213 cell 1.24 m, middle.	55
19. PSD for NE224 cell 1.24 m, near end.	59
20. PSD for NE224 cell 1.24 m, middle.	61
21. After-pulses in anode signal (a), singly differentiated dynode signal (b), and doubly differentiated dynode signal (c) with 1 μ sec delay line shaping.	63

Figure		Page									
22.	After-pulses in singly differentiated dynode pulse (a), and doubly differentiated dynode signal (b), with 400 nsecs delay line shaping.	65									
23.	PSD spectra with 1 μ sec double delay line shaping (a), PSD spectra with 400 nsecs double delay line shaping.	66									
E1.	Details of scintillator cell with dimensions	81									
	<table> <tr> <td><u>D</u></td> <td><u>a</u></td> <td><u>t</u></td> </tr> <tr> <td>45 \pm 1 mm</td> <td>2.0 \pm 0.2 mm</td> <td>2 mm</td> </tr> <tr> <td>22.0 \pm .6 mm</td> <td>1.5 \pm 0.2 mm</td> <td>2 mm</td> </tr> </table> <p>constructed of Pyrex glass.</p>	<u>D</u>	<u>a</u>	<u>t</u>	45 \pm 1 mm	2.0 \pm 0.2 mm	2 mm	22.0 \pm .6 mm	1.5 \pm 0.2 mm	2 mm	
<u>D</u>	<u>a</u>	<u>t</u>									
45 \pm 1 mm	2.0 \pm 0.2 mm	2 mm									
22.0 \pm .6 mm	1.5 \pm 0.2 mm	2 mm									
E2.	Photograph of scintillator cell and laser setup.	82									
E3.	Transmitted light intensity vs. path length for NE213.	83									
E4.	Transmitted light intensity vs. path length for NE224.	84									
E5.	The setup for measurements of the "wavelength-averaged attenuation length".	87									
E6.	Block diagram of the electronics for measurements of the "wavelength-averaged attenuation length".	88									
E7.	Compton edge channel vs. path length for NE213 in the unpainted 45 mm and 22 mm cell (darkened line indicated region over which the least squares fit was performed).	91									
E8.	Compton edge channel vs. path length for NE213 in the black painted 45 mm and 22 mm cells (darkened line indicated region over which the least-squares fit was performed).	97									

I. INTRODUCTION

Neutron time-of-flight detectors typically employ liquid organic scintillators due to their fast response which gives good time resolution. They are, however, as most scintillators, sensitive not only to neutrons but also to gamma-rays. It is necessary to discriminate between the two. Liquid organic scintillators such as NE213 and NE224¹ provide a means of accomplishing discrimination due to their differing responses to neutron and gamma-ray induced scintillations. These responses and their origins will be discussed.

The quality of neutron/gamma-ray discrimination depends on many factors. Among these are the purity of the scintillator, light collection in the detector, optimization of the electronics, system noise, and the properties of the scintillator itself.

It is the hope of this thesis to show the theory behind neutron gamma-ray pulse shape discrimination, and to provide the information necessary to design good pulse shape discrimination into a neutron time-of-flight detector. This will be done by investigating the factors mentioned and testing them on a detector system designed with these factors in mind.

2. Theory of Pulse Shape Discrimination

2.1. Excitation Process and Decay

Liquid organic scintillators, as used in neutron/gamma-ray discrimination, are a two part system. They consist of a solvent, which is the primary energy absorber of the nuclear radiation, and a solute, which is efficient in accepting the energy from the solvent and converting it into photons. The scintillators NE213 and NE224, which are discussed here, are xylene and pseudo cumene solvent based scintillators respectively. These two solvents are used because they have low lying energy levels, and non-bonding electrons (π) which need little energy to attain higher energy levels.² Also, these higher levels are long lived compared to the migration time of the excitation between the solvent and solute. This is necessary if the solute is to be efficient in converting the absorbed energy into photons.

The solvent molecule, after ionization by radiation, recombines with an electron and forms a neutral molecule in an excited state. Generally, these are the upper excited singlet states S_3 , S_2 and S_1 . The S_1 excited state is the state of primary interest, since this is the level that is involved in the transfer of energy from the solvent to the solute, at normal solute concentrations. The upper excited singlet states are depopulated through internal conversion

and other deexcitation processes. Most of the S_1 states are produced directly by ion recombination. For p-xylene based scintillators, approximately 43% of the S_1 states are produced by internal conversion of the S_3 states.³ The S_1 states then transfer their energy to the solute promoting it to its excited singlet state F_1 as shown in the energy level diagram of Figure 1.

An excited triplet state T_1 can also be formed. However, since the transition $S_0 \rightarrow T_1$ requires a change of spin, it is not very likely to occur. Instead an S_1 state is formed which undergoes an intersystem crossing to the T_1 state shown in the energy level diagram of Figure 2. In the intersystem crossing process the S_1 state interacts to produce the T_1 state. Therefore, the yield of the T_1 states is proportional to the density of S_1 states which is in turn proportional to the ionization density. The $T_1 \rightarrow S_0$ transition, also being forbidden, is unlikely to occur. When two T_1 states interact an intersystem crossing occurs yielding an excited singlet state, $T_1 + T_1 \rightarrow S_1 + S_0$. This S_1 state then in turn transfers its energy to the solute producing the scintillation.⁴ The time for the decay then is long compared to that of the $S_1 \rightarrow S_0$ transition since the $T_1 + T_1 \rightarrow S_1 + S_0$ transition depends on the migration time of the molecules in the T_1 state. The $S_1 \rightarrow S_0$ decay has a mean life on the order of 4 nsecs. The $T_1 \rightarrow S_0$ decay has a mean life time of the order of 100 nsecs.

When the scintillator is used for neutron/gamma-ray discrimination, the neutron produces an ionization track by

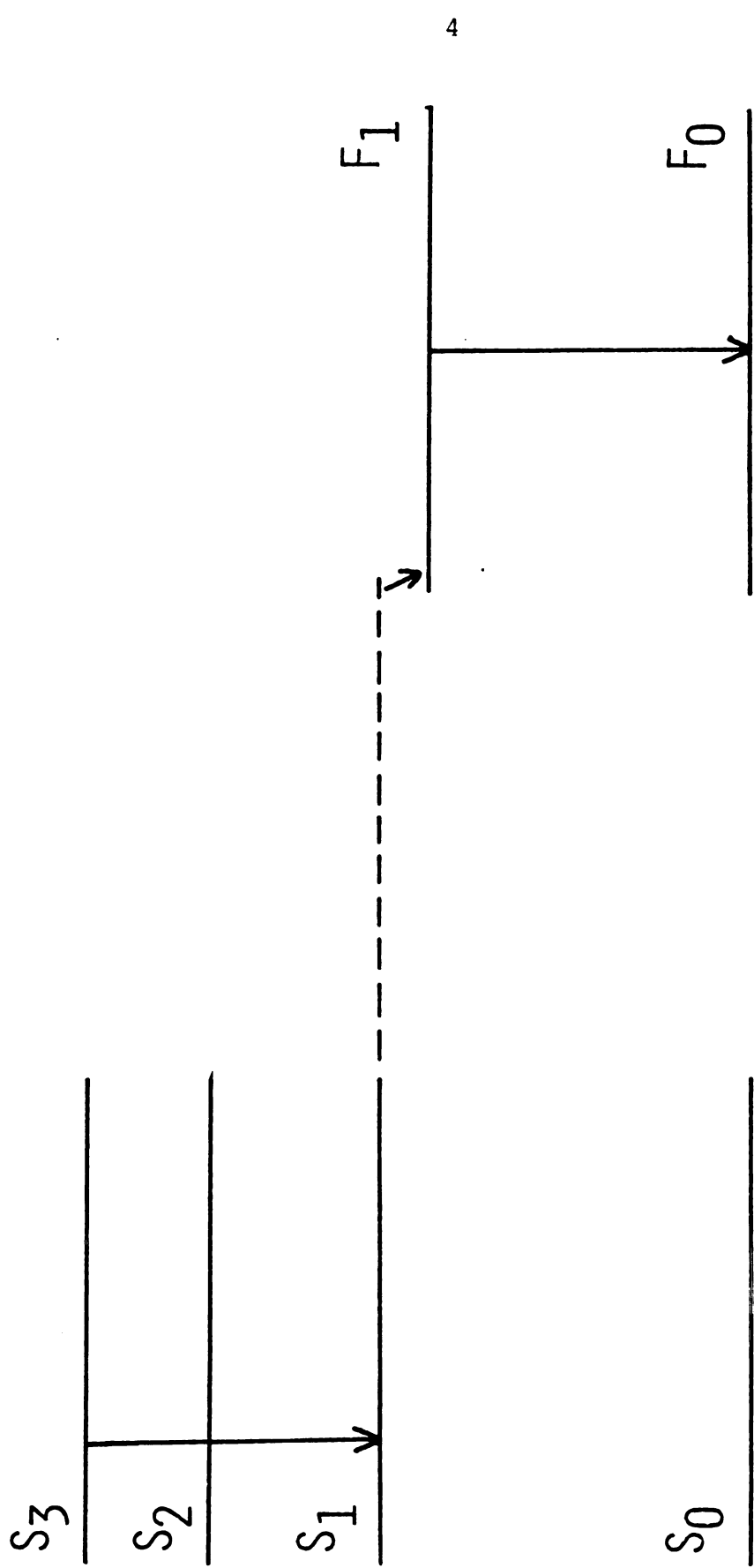


Figure 1. Energy transfer process from solvent to solute.

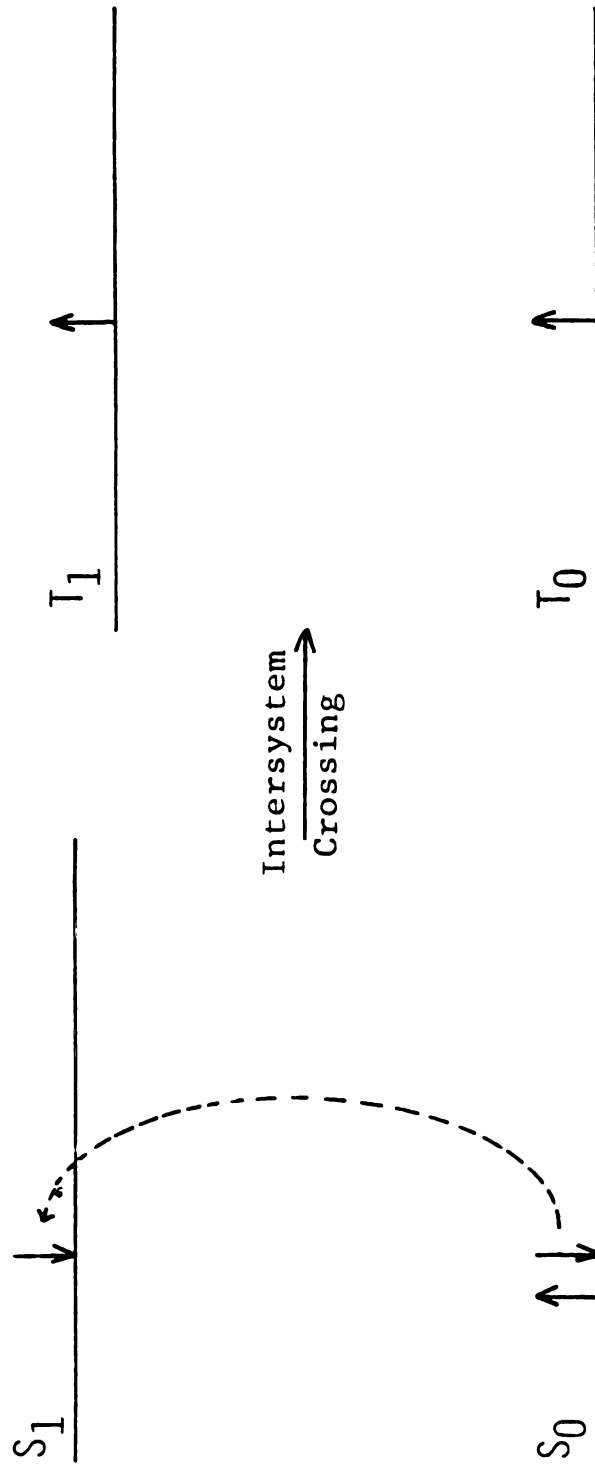


Figure 2.: Production of T_1 states. The arrow represents the spin of the electron.

elastically scattering a proton. A gamma-ray, on the other hand, Compton scatters an electron. The difference in the ionization densities of the two particles then forms the basis for distinguishing whether a neutron or a gamma-ray has been detected, since the light decay of the scintillation will have a different shape. The photon number per unit time for the electron and proton, respectively, are then generally considered to be given by:⁵

$$(1) \quad A_e(t) = (A_{ef} \exp(-t/\tau)/\tau + A_{es} \exp(-t/\tau_{es})/\tau_{es}),$$

$$(2) \quad A_p(t) = (A_{pf} \exp(-t/\tau)/\tau + A_{ps} \exp(-t/\tau_{ps})/\tau_{ps}),$$

where A_{ef} and A_{pf} are the relative contributions of the fast part of the decay produced by the electron and proton respectively. A_{es} and A_{ps} are the relative contributions of the slow part of the decay of the scintillation. τ is the fast decay time for both the proton and electron induced scintillations. τ_{es} and τ_{ps} are the slow decay times for the electron and proton induced scintillations. $A_e(t)$ and $A_p(t)$ are normalized such that $\int_0^{\infty} A(t) dt = 1$.

2.2. Zero-Crossover Technique

The zero-crossover technique measures the time it takes for the linear signal from the photomultiplier to reach one half of its peak value. The block diagram in Figure 3 shows one method of measuring this time.

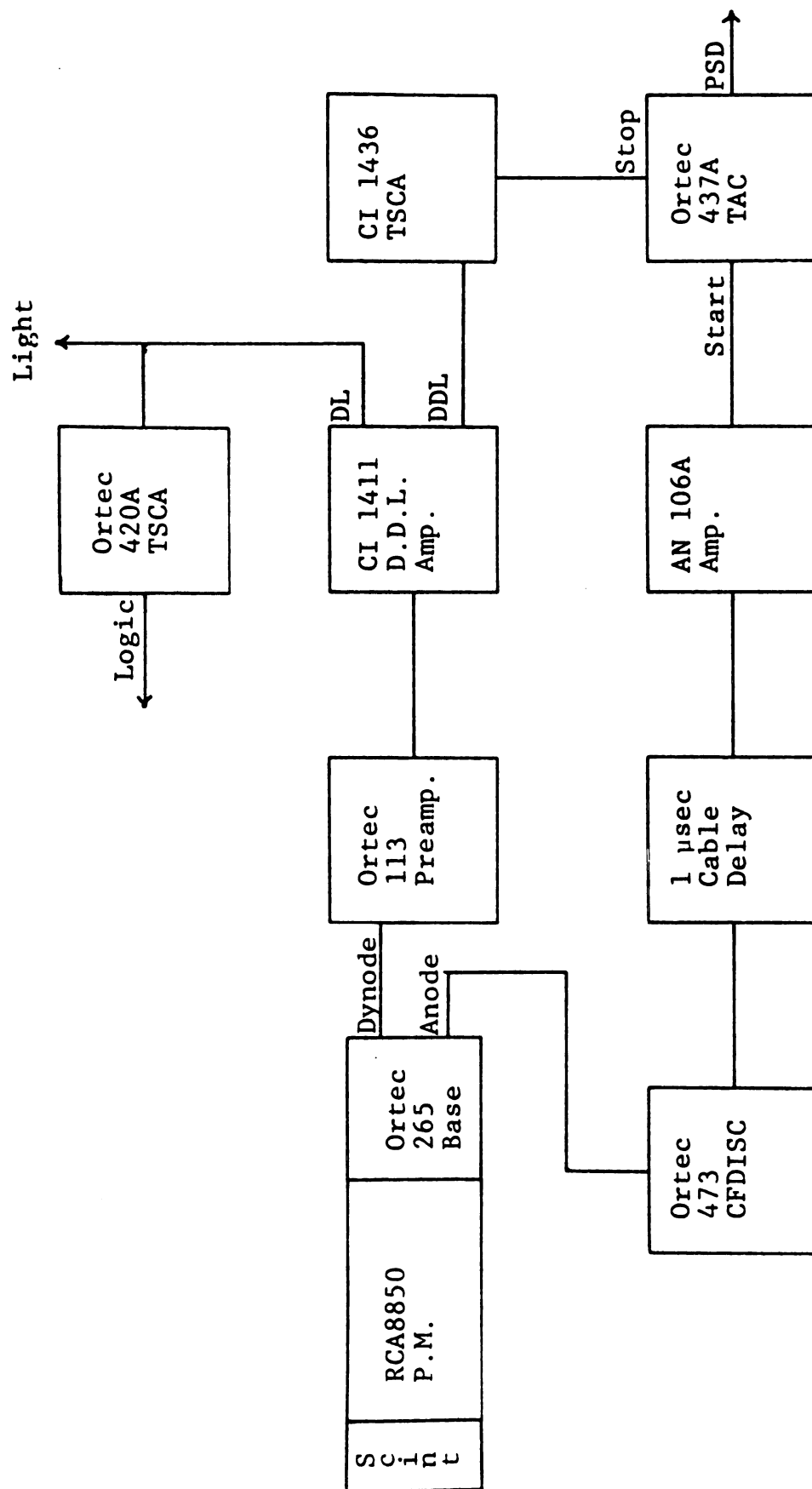


Figure 3. Block diagram of pulse shape discrimination electronics.

The anode signal from an RCA 8850 photomultiplier provides a fast start signal which is passed into an ORTEC 473 constant fraction discriminator. The constant fraction discriminator provides a signal when the anode pulse reaches a fixed fraction of its peak value, thus reducing time jitter due to amplitude variation. This signal is then delayed by cable to compensate for other circuit delays and fed to the start input of an ORTEC 437A time to amplitude converter.

The linear dynode signal is amplified by an ORTEC 113 preamplifier and sent through a Canberra 1411 double delay line amplifier. The double delay line amplifier first delays the incoming pulse 1 μ sec., inverts it, and adds it to the original pulse, thus producing a unipolar pulse of 1 μ sec. duration, as shown in Figure 4a. The trailing edge is an inverted image of the leading edge. This unipolar pulse is further delayed 1 μ sec., inverted, and added to the original unipolar pulse as in Figure 4b. This produces a bipolar pulse which crosses through zero at approximately 1 μ sec. plus the time it takes for the original signal to reach 1/2 peak value.⁶ This zero-crossing time is determined by a Canberra 1436 timing single channel analyzer in the zero crossing mode. The fast signal from the timing single channel analyzer is used as a stop signal for the time to amplitude converter.

The output of the time to amplitude converter is then related to the rate of decay of the scintillation. To know exactly how it relates we must know what happens to the

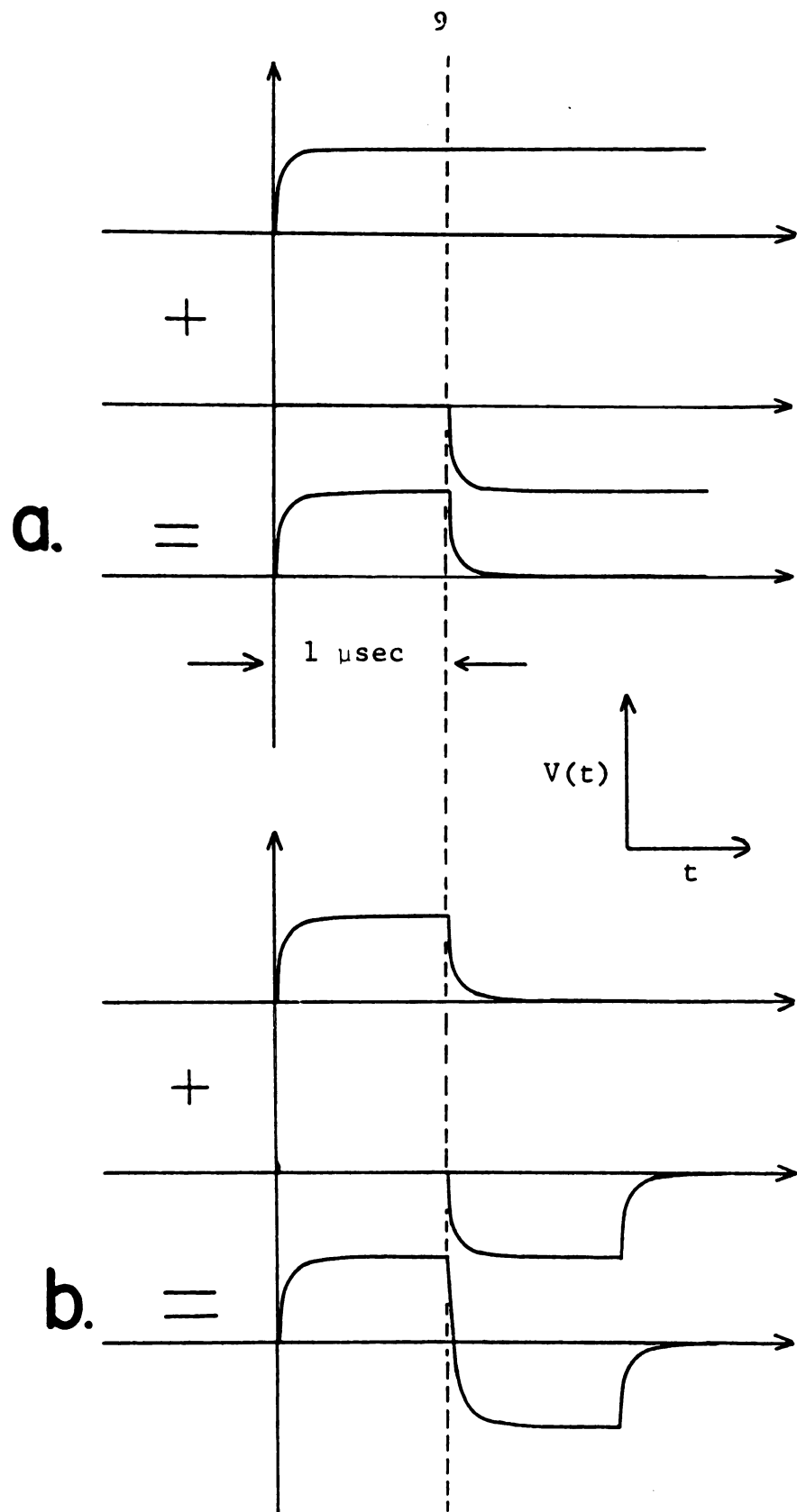


Figure 4. Unipolar and bipolar pulse shaping.

original light pulse as it is detected and the resulting signal passes through the system.

2.3 Model of System Performance

Let us choose the case of the electron induced scintillation. The current output of the dynode will then be

$$(3) \quad i(t) = A_e(t) PGq,$$

where P is the number of photoelectrons produced at the photocathode and G is the multiplier gain.⁷ Since G is constant it will be considered to be one. Therefore, if at time $t=0$ a light pulse occurs at the dynode, the voltage $V(t)$ at time t is given by

$$(4) \quad V(t) = R \int_0^t i(t') g(t, t') dt',$$

where $g(t, t')$ is the transfer function of the RC dynode circuit, a portion of which is shown in Figure 5. The transfer function for this circuit is⁸

$$(5) \quad g(t, t') = \begin{cases} 1/(RC) \exp(-(t-t')/(RC)) & \text{for } t \gg t' \\ 0 & t \gg t' \end{cases}.$$

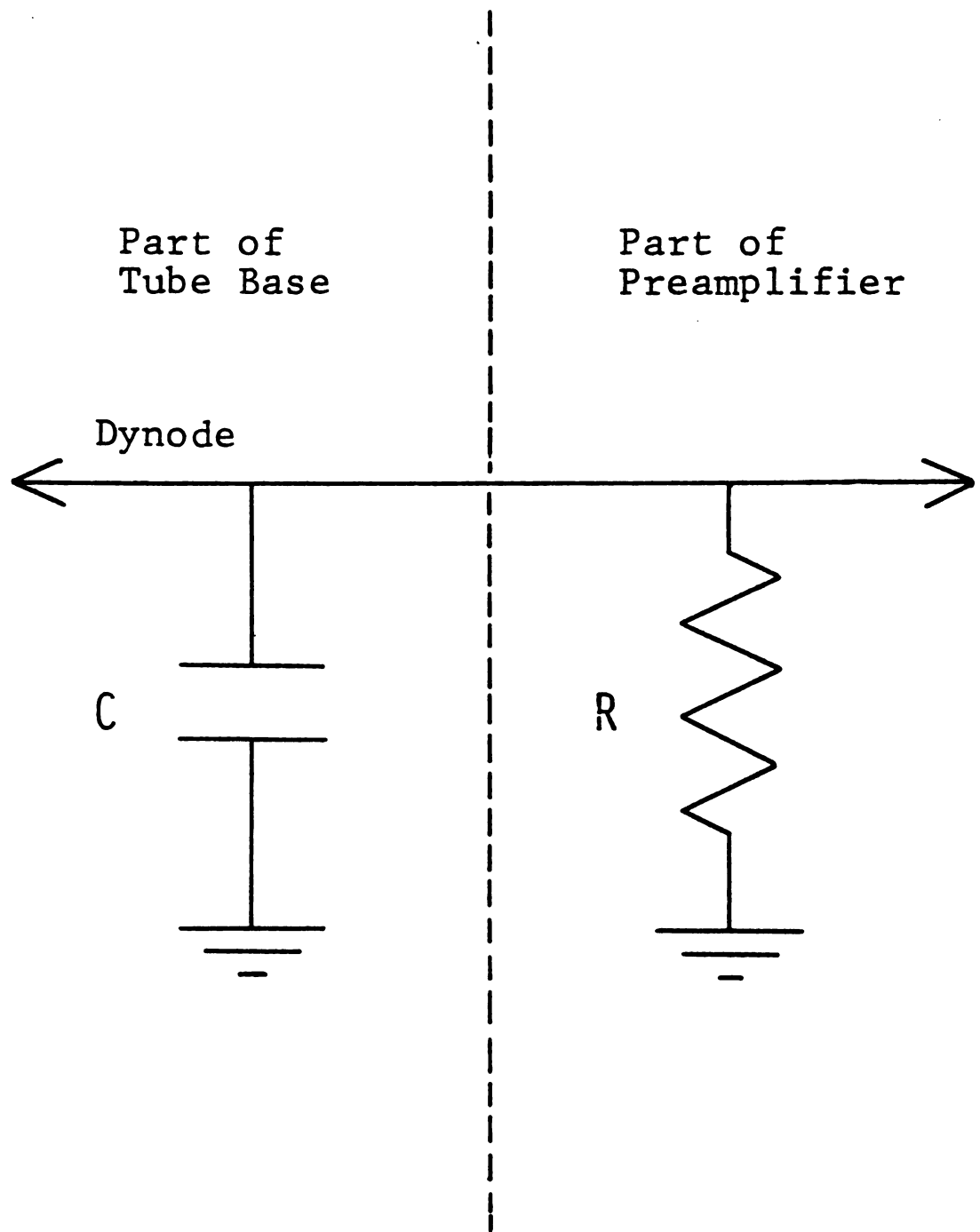


Figure 5. RC shaping circuit for dynode pulse

Performing the integral in equation 4 then yields

$$(6) \quad V(t) = \frac{Pg}{C} \left[\frac{A_{ef}}{\left[\frac{\tau}{RC} - 1 \right]} \left[\exp \left(-\frac{t}{\tau} \right) - \exp \left(-\frac{t}{RC} \right) \right] + \frac{A_{es}}{\left[\frac{\tau_{es}}{RC} - 1 \right]} \left[\exp \left(-\frac{t}{\tau_{es}} \right) - \exp \left(-\frac{t}{RC} \right) \right] \right].$$

Since RC is typically several orders of magnitude larger than τ_{es} or τ and much larger than the time t at which $V(t)$ is evaluated, equation 6 may be simplified to

$$(7) \quad V(t) = \frac{Pg}{C} \left[A_{ef} \left[1 - \exp \left(-\frac{t}{\tau} \right) \right] + A_{es} \left[1 - \exp \left[-\frac{t}{\tau_{es}} \right] \right] \right]$$

To find the distribution of $V(t)$ we can first find the distribution for the integral light output $N=Pf(t)$ given by

$$(8) \quad N=Pf(t) = \int_0^\infty P A_e(t) dt.$$

Integrating yields

$$(9) \quad Pf(t) = P \left[A_{ef} \left[1 - \exp \left(-\frac{t}{\tau} \right) \right] + A_{es} \left[1 - \exp \left[-\frac{t}{\tau_{es}} \right] \right] \right].$$

Since the number of photoelectron N arriving at time $t=T$ has a Poisson distribution about the average value P , we can assume that the probability that the N th pulse arrives between time 0 and t is given by the Poisson distribution⁹

$$(10) \quad P_N(t) = \frac{\exp(-Pf(t)) [Pf(t)]^N}{N!} Pf(t) \quad .$$

Note that equation 6 can be expressed, by using equation 9, as

$$(11) \quad V(t) = \frac{Pq}{C} f(t) \text{ or } \frac{Nq}{C} \quad .$$

Since $V(t)$ and $N(t)$ only differ by a constant factor the same distribution holds for $V(t)$, namely,

$$(12) \quad P_V(t) = \frac{\exp \left[-\frac{CV(t)}{q} \right] \left[\frac{CV(t)}{q} \right]^N \left[\frac{CV(t)}{q} \right]}{N!} \quad .$$

The probability that the voltage has reached a value of $V(t)$ between t and $t+dt$ is

$$(13) \quad P_V(t)dt = \frac{\exp \left[-\frac{CV(t)}{q} \right] \left[\frac{CV(t)}{q} \right]^N \left[\frac{C\dot{V}(t)}{q} \right]}{(N-1)!} \quad .$$

This, as stated earlier, assumes a Poisson distribution of the Pulse of P photoelectrons. This, in turn, implies the voltage pulse V is normally distributed about the average value of V at time $t=T$. If the voltage is to be exactly $V(t)$ then the pulse must have P photoelectrons so that $(P-N)$ photoelectrons must arrive in the remaining time $T-t$. Then a similar derivation as for equation 13 yields the probability for this to happen as

$$(14) \quad P_{V-V(T)}(T-t) = \frac{\exp \left[-\left[1 - \frac{CV(t)}{q} \right] \right] \left[1 - \frac{CV(t)}{q} \right]^{P-N}}{(P-N)!} \quad .$$

Thus, the combined probability $P_{V,V(T)}(t)dt$ that the voltage reaches $V(t)$ between t and $t+dt$ in a voltage pulse of exactly $V(T)$ is

$$(15) \quad P_{V,V(T)}(t)dt = P_V \cdot P_{V(T)}(T-t) \quad \text{or}$$

$$\frac{\exp(-1) \left[1 - \frac{CV(t)}{q} \right]^{P-N} \left[\frac{CV(t)}{q} \right]^{N-1} \dot{V}(t)}{(N-1)! (P-N)!} dt$$

This is equivalent to the treatment by Kuchnir and Lynch.¹⁰

For a fixed fraction k , $V(t)=KV(T)$, or $N=kP$, the mean time at which this occurs is

$$(16) \quad \bar{t} = \frac{\int_0^T t P_{V,V(T)}(t) dt}{\int_0^T P_{V,V(T)}(t) dt},$$

and the variance of t is

$$(17) \quad \epsilon_e^2 = \langle t_e^2 \rangle - \bar{t}_e^2 = \frac{\int_0^T t^2 P_{V,V(T)}(t) dt}{\int_0^T P_{V,V(t)} dt} - \bar{t}^2$$

A similar derivation yields the same result for the proton induced scintillation.

One method of characterizing the ability to distinguish pulse shape is the figure of merit D defined by

$$(18) \quad D = \frac{\bar{t}_e - \bar{t}_p}{\epsilon},$$

where $\sigma^2 = \sigma_e^2 + \sigma_p^2$.¹¹ In practice, one measures the figure of merit M defined by the relation

$$(19) \quad M = \frac{t_e - t_p}{\text{sum of FWHM}}.$$

If the t distribution were Gaussian, then $2.36M \leq D \leq 3.34M$.¹²

2.4. Calculation of System Performance.

The figure of merit D can be calculated from various levels of photoelectron numbers, and the fraction of pulse height at which one chooses to measure the time difference of the proton and electron induced scintillation by evaluating equation 18. First, expanding equation 16 one obtains

$$(20) \quad t = \frac{\int_0^T t \left[1 - A_{ef} \left[1 - \exp \left[-\frac{t}{\tau} \right] \right] + \frac{A_{es} \left[1 - \exp \left[-\frac{t}{\tau_{es}} \right] \right]^{P-N} X}{A_{es} \left[1 - \exp \left[-\frac{t}{\tau_{es}} \right] \right]^{P-N} X} \right] dt}{\int_0^T \left[1 - A_{ef} \left[1 - \exp \left[-\frac{t}{\tau} \right] \right] + \frac{A_{es} \left[1 - \exp \left[-\frac{t}{\tau_{es}} \right] \right]^{P-N} X}{A_{es} \left[1 - \exp \left[-\frac{t}{\tau_{es}} \right] \right]^{P-N} X} \right] dt}$$

$$\frac{\left[A_{ef} \left[1 - \exp \left[-\frac{t}{\tau} \right] \right] + A_{es} \left[1 - \exp \left[-\frac{t}{\tau_{es}} \right] \right] \right]^{N-1} X}{\left[A_{ef} \left[1 - \exp \left[-\frac{t}{\tau} \right] \right] + A_{es} \left[1 - \exp \left[-\frac{t}{\tau_{es}} \right] \right] \right]^{N-1} X}$$

$$\frac{\left[\frac{A_{ef}}{\tau} \exp \left[-\frac{t}{\tau} \right] + \frac{A_{es}}{\tau_{es}} \exp \left[-\frac{t}{\tau_{es}} \right] \right] dt}{\left[\frac{A_{ef}}{\tau} \exp \left[-\frac{t}{\tau} \right] + \frac{A_{es}}{\tau_{es}} \exp \left[-\frac{t}{\tau_{es}} \right] \right] dt} .$$

A similar result for \bar{t}^2 is obtained by changing the first t to a t^2 in the top integral. One could find an analytical solution if t were assumed to approach infinity. However, little insight would be gained from a very tedious task. Instead equations 16, 20 and 18 were evaluated using the program listed in Appendix A, on an XDS Sigma 7 computer located at Michigan State University's Cyclotron Laboratory. The values of A_{es} , A_{ef} , A_{ps} , A_{pf} , τ , τ_{ef} listed in Table 1 were obtained from the paper by Sabbah and Suhami.¹³ These were used in all of the following calculations. Table 2 lists the results as a function of the photoelectron number P for a fixed fraction of pulse height. The constant k was chosen to be 0.5. Since the distribution is Poisson, the figure of merit D should increase as the square root of P . Inspection of Table 2 shows the expected increase in the figure of merit as the photoelectron number is increased.

One is also interested in the actual appearance of the pulse shape signatures. These were obtained by summing the probability distributions for the electron and proton induced scintillations assuming an equal photoelectron yield for both types of scintillations. The program listing for this is in Appendix B. Figure 6 shows the expected pulse shape signatures as a function of increasing photoelectron number.

Table 1. Data for Decay Times and Relative Contributions
from Sabbah and Suhami.¹³

$A_{ef} = 0.5$	$\tau_{ef} = 4 \text{ nsecs}$
$A_{es} = 0.5$	$\tau_{es} = 25 \text{ nsecs}$
$A_{pf} = 0.8$	$\tau_{pf} = 4 \text{ nsecs}$
$A_{ps} = 0.2$	$\tau_{ps} = 47 \text{ nsesc}$

The fraction of the integrated pulse height at which one chooses to do the timing affects the figure of merit. For a fixed number of photoelectrons, 300, the figure of merit was calculated for various values of k using the program listed in Appendix C. The results are graphed in Figure 7. One can see that the best discrimination between the electron and proton induced scintillation occurs at $k=0.87$. This treatment assumes no system noise.

Inspection of Equation 7 shows that the rate of change of the pulse decreases as time increases. The uncertainty of the timing of the signal due to noise jitter is given approximately by

$$(21) \quad \Delta t = \frac{\sqrt{2}G2.35\Delta V}{\left[\frac{dv}{dt}\right] t} ,$$

where G is the delay line amplifier gain, ΔV is the RMS noise at the input, and dv/dt is the time rate of change of the signal of interest.¹⁴ The factor of 2.35 converts from the RMS value to FWHM, and the $\sqrt{2}$ factor occurs because of two level measurements. Thus, as the time rate of change of the signal increases, the timing jitter decreases. Therefore a compromise may have to be made to minimize the effects of amplifier noise and fraction of the pulse height discrimination level on the quality of the pulse shape signature.

Table 2. Theoretical Figure of Merit (D) for a given Number of Photoelectrons (P).

P	D
500	4.74
1,000	6.70
1,500	8.23
2,000	9.50
2,500	10.64
3,000	11.67
3,500	12.56
4,000	13.45
4,500	14.25
5,000	15.04
5,500	15.81
6,000	16.44

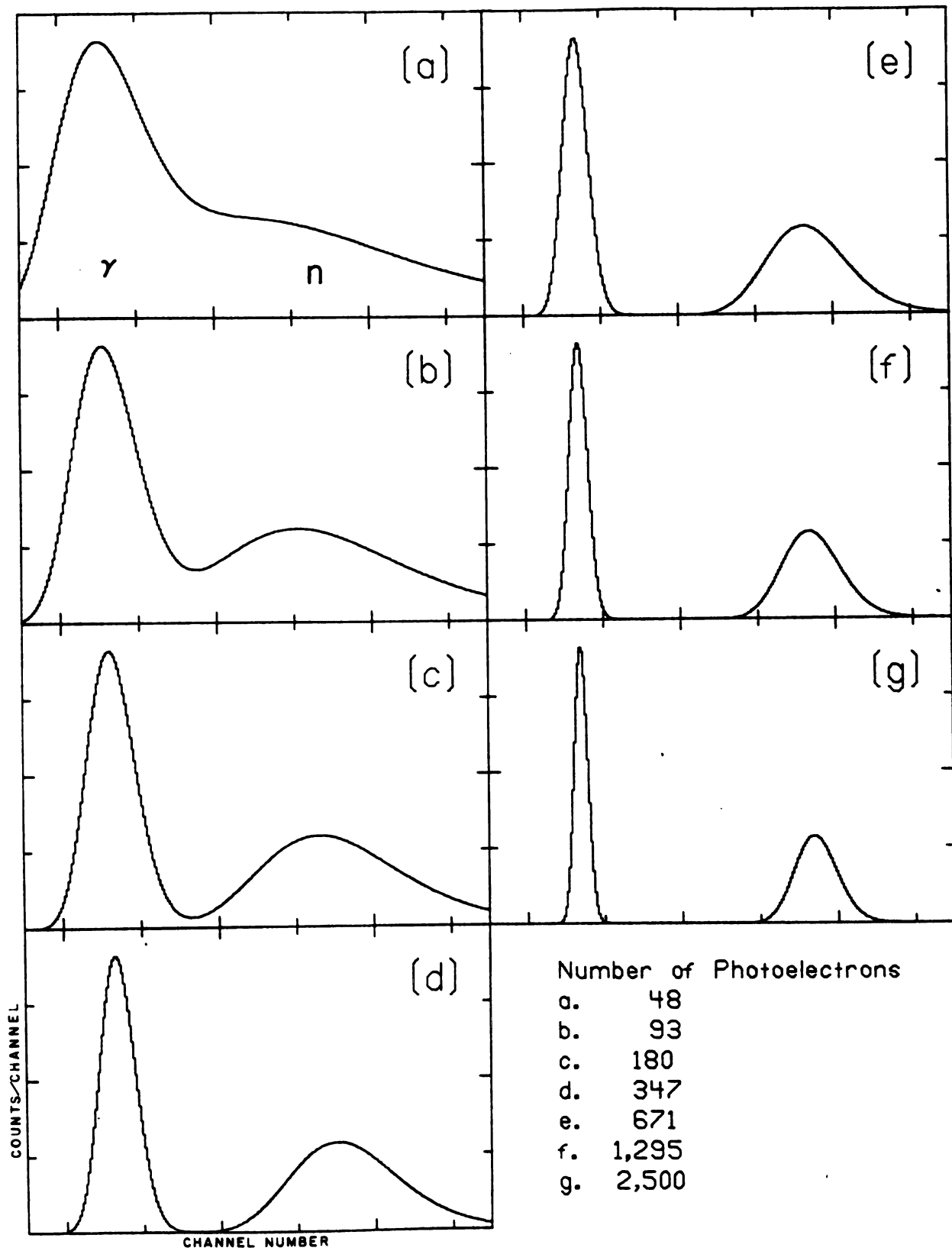


Figure 6. Plots of expected P.S.D. signatures for NE213.

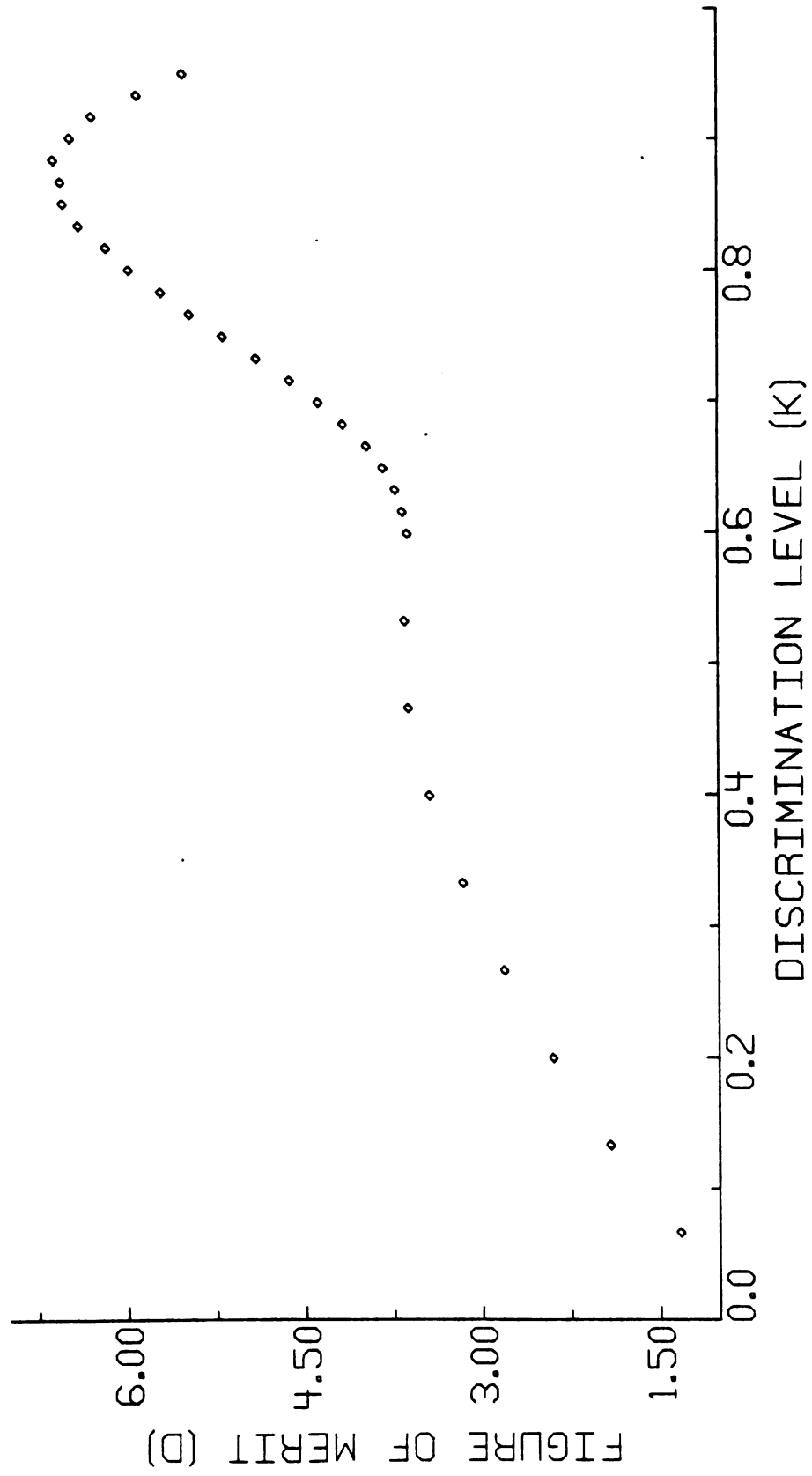


Figure 7. Figure of merit versus discrimination level.

3. FIGURE OF MERIT FOR NE213 AND NE224 UNDER IDEAL CONDITIONS

3.1. NE213

A test cell was constructed of Pyrex glass as shown in Figure 8. The cell was painted with NE560¹⁵ reflector paint to optimize light collection. The cell was cleaned with nitric acid and rinsed with distilled water and allowed to dry. A teflon cap was machined to seal the cell. Teflon was chosen since it is nonreactive and highly insoluble, thus lessening the chances of contamination.

The cell was filled with NE213 and helium gas was then bubbled freely through it for 24 hrs to remove oxygen contamination. After bubbling the cell was capped. Care was taken to ensure that the remaining void was filled with helium.

The cell was then attached to an RCA 8850¹⁶ photomultiplier tube with optical coupling grease. The number of photoelectrons produced per Kev of energy deposited in the scintillator was then measured using the method of Kelley et al.¹⁷ The average number of photoelectrons P in the pulse was taken to be¹⁸

$$(22) \quad P = \left[\frac{I_1}{\sigma} \right]^2 \left[1 + \frac{1.2G}{G_1(G-1)} \right],$$

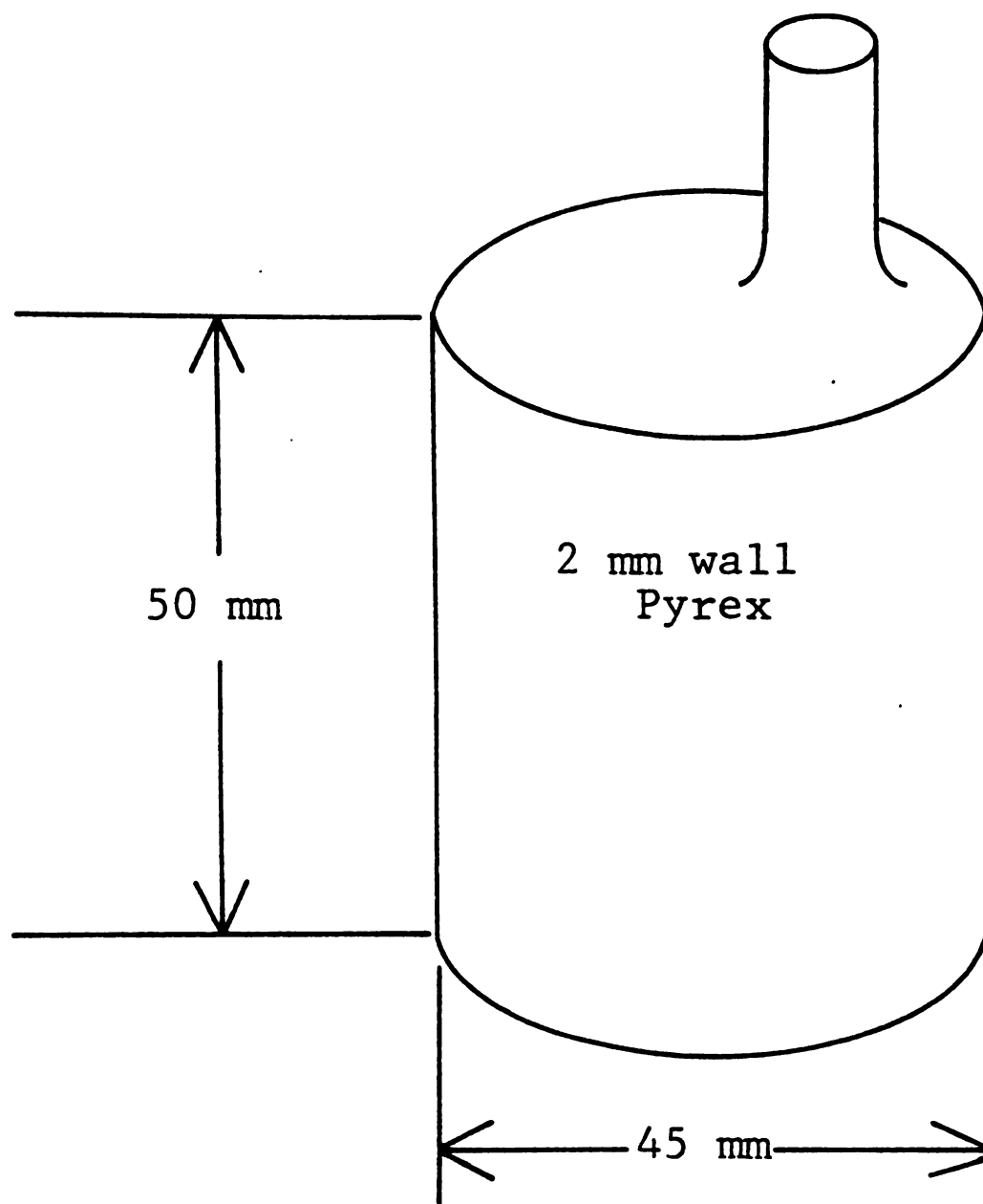


Figure 8. Scintillator cell, 50 mm x 45 mm.

where G_1 is the average gain of the first dynode, G is the average gain of the other dynodes, I_1 is the centroid of the peak in channels, and σ is the standard deviation in channels of the peak. Taking $G_1=5$ and $G=3$ we have $P=1.36(I_1/\sigma)^2$.

If the channel number C of the Compton edge, of known energy, is then measured, the number of photoelectrons per KeV of energy deposited in the scintillator is then

$$(23) \quad P_{el} = \frac{P}{I_1 C} = \frac{1.36 I_1}{C \sigma^2} \quad .$$

A very stable LED light pulser was¹⁹ constructed, the schematic of which is in Figure 9. The LED light pulser provides a very stable pulse, so that the width of the observed peak is due entirely to counting statistics and not due to drifts in the source. The LED pulser was coupled to the same photomultiplier that the NE213 cell was coupled to with a fiber optic light pipe. This allows the measurement of P to be made without disturbing the coupling of the cell to the photomultiplier.

The electronics used are shown in block diagram in Figure 10. The LED light pulser produces a light pulse that is linear with respect to its input trigger pulse amplitude. An Ortec 448 research pulser was used to trigger the LED pulser. The Ortec pulser was set for a decay time constant of 10 μ secs and a rise time of 20 nsecs. The output was adjusted for an LED pulse such that the spectrum's centroid would be roughly equivalent to the ^{60}Co Compton edge. The pole zero of the CI 1411 delay line amplifier

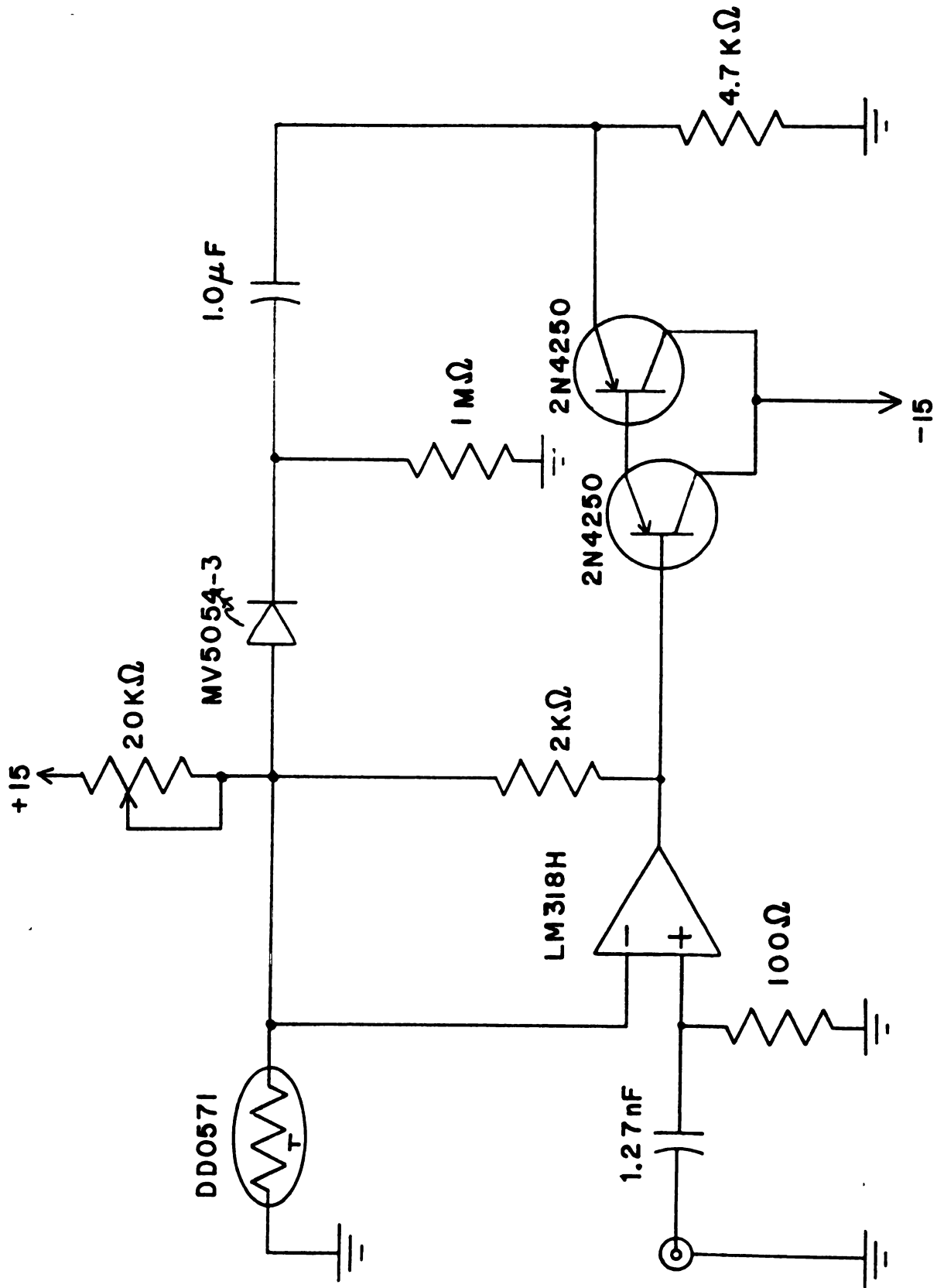


Figure 9. Schematic of LED pulser of Hagen and Eklund.¹⁹

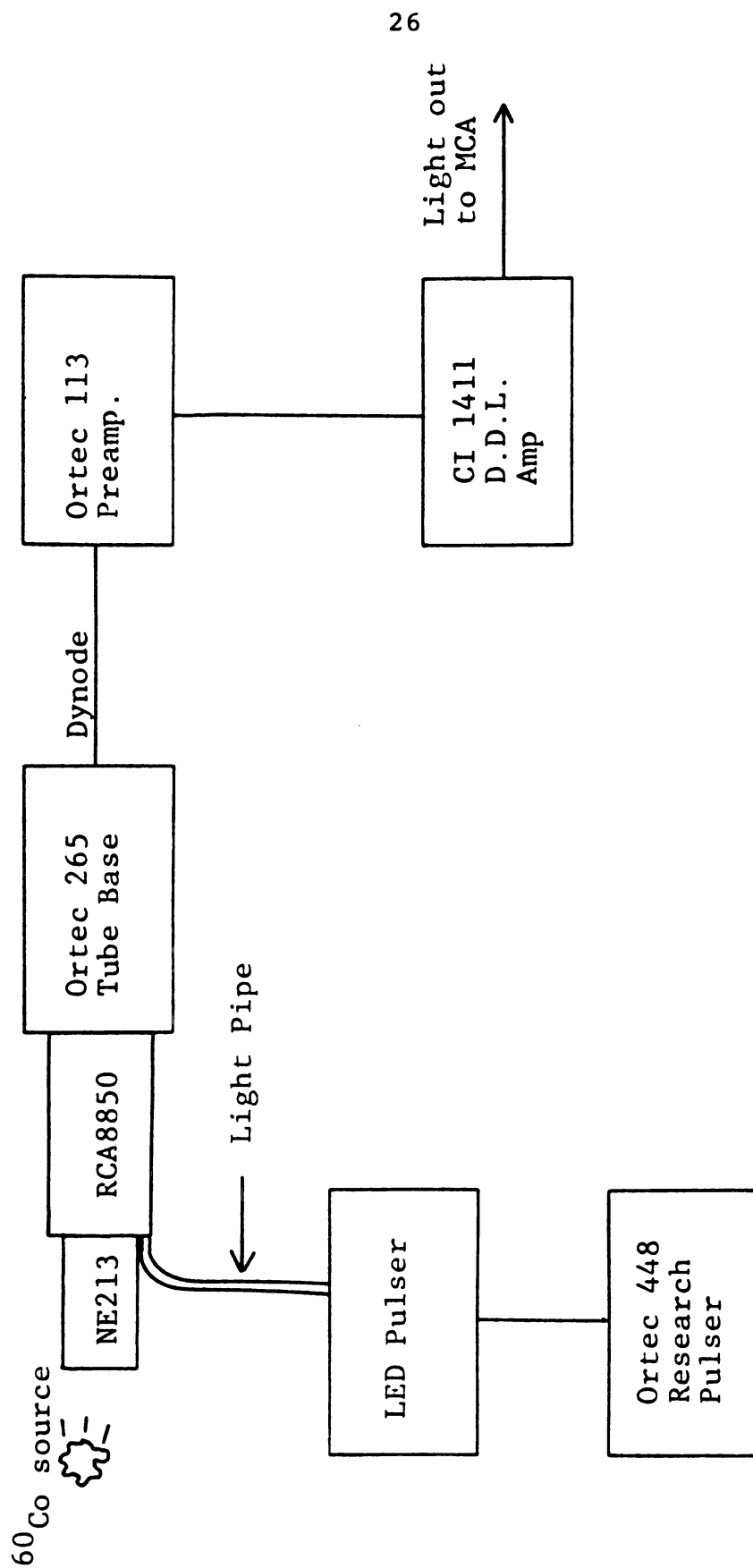


Figure 10. Electronics for determining P_{el} .

was then adjusted so that the trailing edge of the singly differentiated output pulse would return to the baseline.

Spectra were then taken for various settings of the Ortec pulser. The LED pulser was then shut off and a spectrum was taken using the ^{60}Co source. The results are listed in Table 3. For NE213 an average of 1.8 photoelectrons per KeV was obtained for P_{el} .

Using the data in Table 2, and knowing that there are 1.8 photoelectrons per KeV, the expected M value versus equivalent electron energy can be tabulated. This is done in Table 4.

The NE213 scintillator cell was then tested for its neutron/gamma-ray pulse shape discrimination characteristics using the electronics of Figure 3. The system was tuned using a ^{60}Co source. The high voltage for the photomultiplier was set at approximately 1800 volts and the CI 1411 delay line amplifier's pole zero was then adjusted so that the singly differentiated output pulse would return to the baseline with little under or overshoot. The risetime adjustment of the CI1436 timing single channel analyzer was then adjusted for minimum walk. The Ortec 473 constant fraction discriminator was set at the minimum threshold that would not pass noise and was operated in the leading edge node. The light, logic, and PSD signals were routed to a multichannel analyzer system comprised of a PDP 11/45 computer connected to a CAMAC crate. The logic pulse strobes the system and merely tells the computer to look at the light

Table 3. Data for Number of Photoelectrons per KeV for an NE213 Scintillator Mounted on an RCA 8850 Photo-multiplier.

Pulser Setting	Centroid	F.W.H.M.	P_{el} [Photoelectrons/KeV]	
9	979.8	56.0	1.66	
7	896.5	53.5	1.67	
5	774.5	48.1	1.78	P_{el} Avg. 1.8 ± 0.1
3	612.17	41.2	1.92	

Table 4. Theoretical Figure of Merit (M) at a Given Energy for NE213.

Energy [MeV]	Figure of Merit
0.28	1.60
0.57	2.28
0.85	2.75
1.14	3.16
1.42	3.63
1.70	3.97
1.99	4.17
2.27	4.49
2.56	4.88
2.84	5.02
3.13	5.34
3.41	5.69

and PSD signals. The system is capable of collecting the PSD spectra gated by light levels set by software.

After tuning the system, the spectra of the ^{60}Co Compton edge were collected to calibrate the channel numbers in term of equivalent electron energy deposited in the scintillator. Then a PuBe neutron and gamma-ray source was placed in position and spectra of the PSD signal, gated by various light levels, were taken. The results are shown in Figure 11 for various energies. The FWHM of the peaks and the centroids were obtained using the program BKANAL on the PDP 11/45. The background was not subtracted. In practice this cannot be done in real time; hence it is more meaningful to leave it in. The figure of merits are tabulated in Table 5.

The figure of merit for an equivalent electron energy range of 1.1 to 1.4 MeV was found to be 1.7. This is less than the predicted value of 3.2 at 1.14 MeV, which however does not include the contribution due to system noise. Thus the actual value should be expected to be less than that predicted. R. A. Winyard et al.²⁰ found M to be 3.1 for NE213 at an energy range of 0.91 to 1.1 MeV. Winyard's value for M at this energy may be higher due to reduced noise. However, it had been assumed, in this thesis, that the values of A_{es} , A_{ef} , A_{ps} , A_{pf} were independent of energy. This is clearly not the case, since the ionization density changes as a function of the energy of the ionizing particle. The history of the NE213 was not known either. Although care was taken to deoxygenate the scintillator, it may have

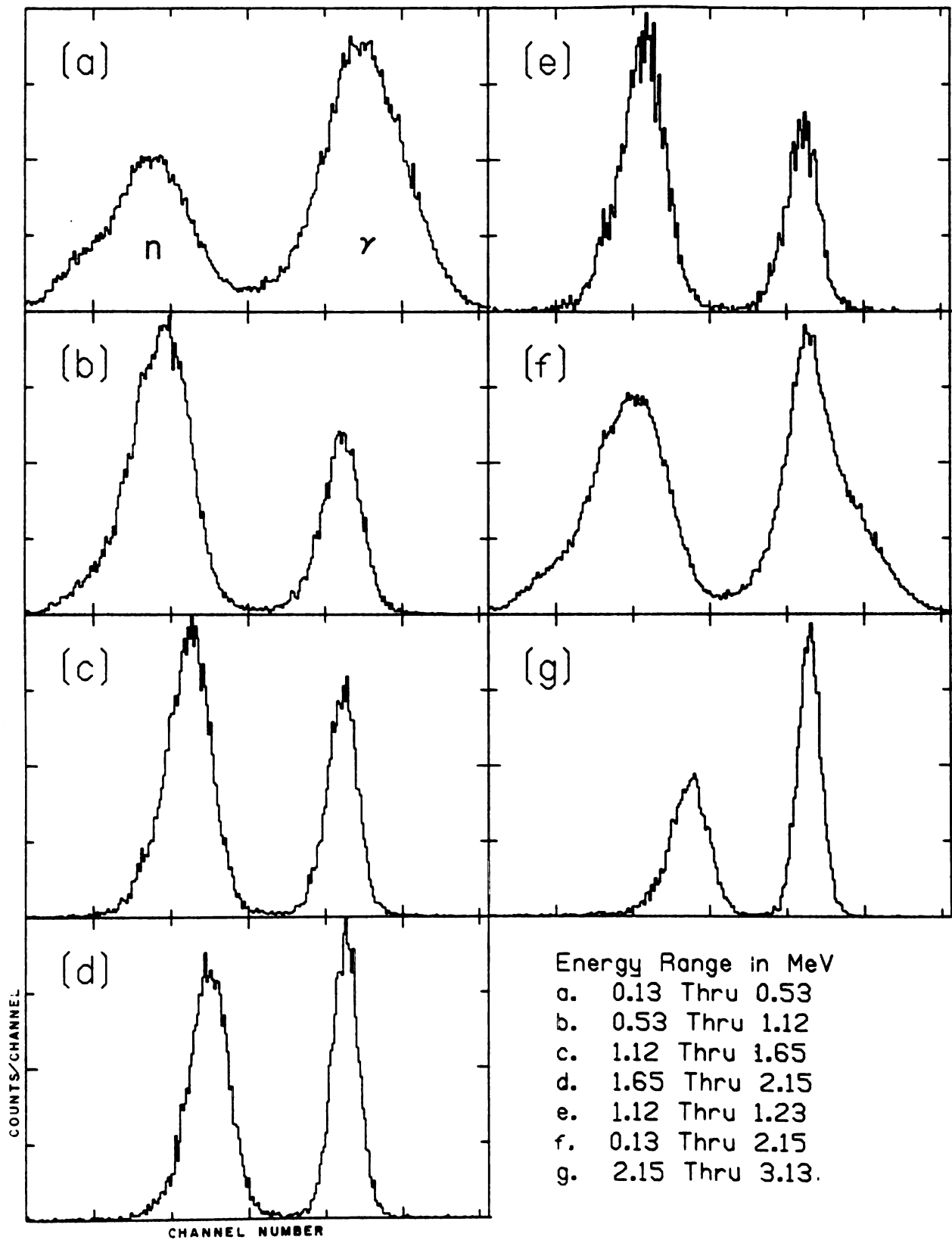


Figure 11. NE213 P.S.D. spectra 45 mm X 50 mm cell.

Table 5. Figure of Merit (M) for an 45 mm x 50 mm NE213 Scintillator

Energy Range [MeV]	Figure of Merit
0.13 thru .53	1.11
0.53 thru 1.12	1.47
1.12 thru 1.65	1.65
1.65 thru 2.15	1.71
1.12 thru 1.23	1.71
0.13 thru 2.15	1.62
2.15 thru 3.13	1.69

contained some impurities which could quench the desired triplet states. Oxygen is just one such impurity, although probably the most common.

3.2. Figure of Merit for NE224

Since there is little reliable data for NE224 concerning its decay modes and the relative contributions of these modes, its theoretical figure of merit cannot be calculated. The figure of merit versus energy was measured using an identical cell and electronics following the method of Section 3.1. The PSD spectra are shown in Figure 12 and the figures of merit are listed in Table 6. For an electron equivalent energy range of .62 to 1.24 MeV a figure of merit of 1.23 was obtained. This is less than that of NE213, but NE224 still gives reasonable pulse shape discrimination. Less attenuation of the light collected can be tolerated for NE224 since the figure of merit is less to start with. This will be seen in Section 4.

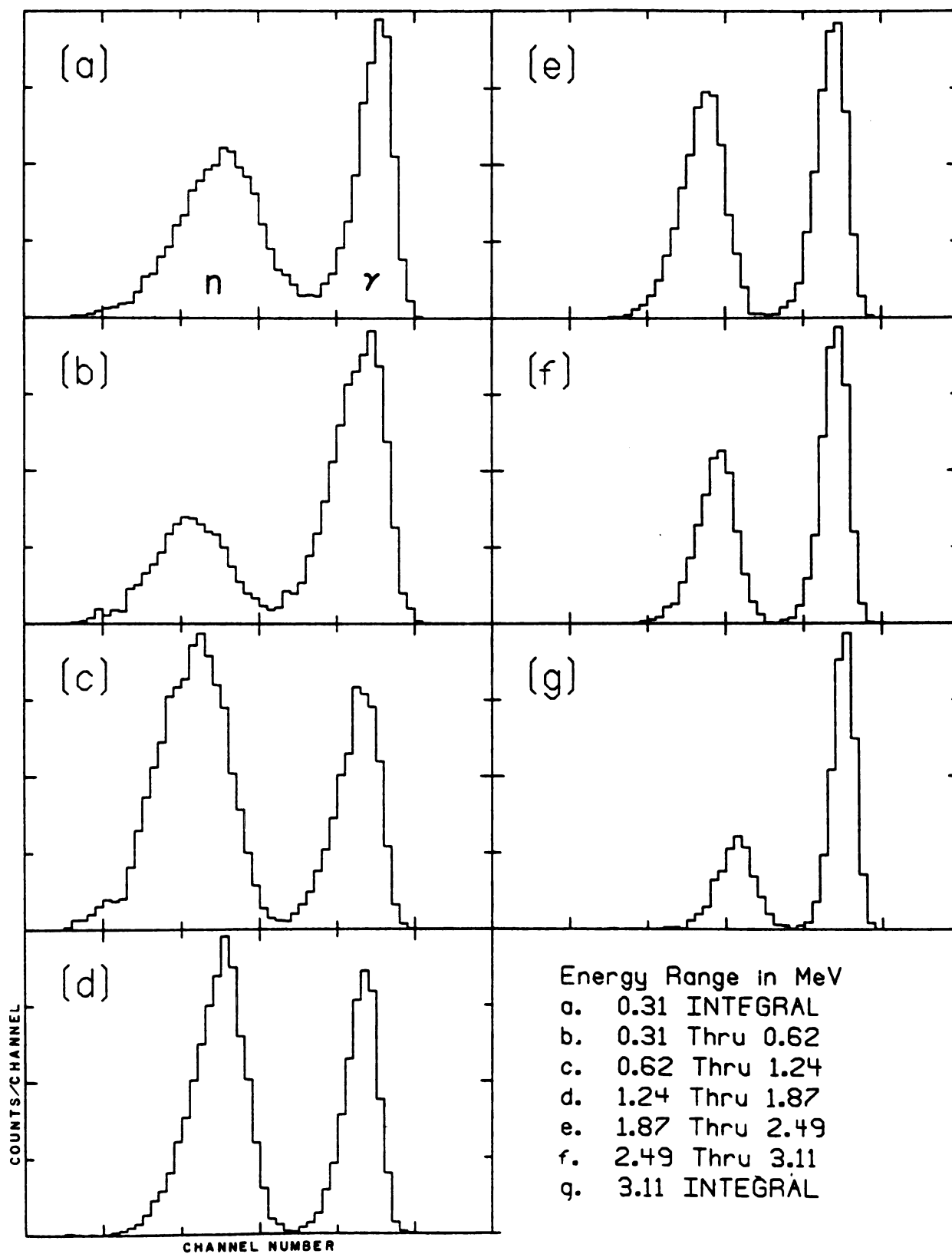


Figure 12. NE224 P.S.D. spectra 45 mm X 50 mm cell.

Table 6. Figure of Merit (M) for a 45 mm x 50 mm NE224 Scintillator.

Energy Range [MeV]	Figure of Merit
0.31 Integral	1.08
0.31 thru .62	1.12
0.62 thru 1.24	1.23
1.24 thru 1.87	1.35
1.87 thru 2.49	1.46
2.49 thru 3.11	1.62
3.11 Integral	1.57

4. LIGHT COLLECTION IN THE SCINTILLATION COUNTER

4.1. Effects of Light Attenuation on Figure of Merit

The figure of merit M defined by Equation 19 is inversely proportional to the sum of the FWHM of the distributions for the electron and proton induced scintillations. The FWHM of the distributions are in turn equal to $\epsilon/2.36$. The standard deviation of the distribution is, by Equation 12, inversely proportional to the square root of the total photoelectron number P . Therefore

$$(24) \quad M \propto \frac{1}{\sqrt{P}} \quad .$$

It is then clearly desirable to make as many photoelectrons as possible by collecting as much of the light produced by the scintillations as is possible.

4.2. Light Collection Problems with a Large Volume Neutron Time-of-Flight Detector

The large neutron time-of-flight detector at Michigan State University Cyclotron Laboratory consists of an 84 cm by 13 cm x 2.5 cm (inside dimensions) cell constructed of plexiglass G, filled with NE224. A light pipe placed at each end couples to an RCA 8850 photomultiplier tube (Figure 13).

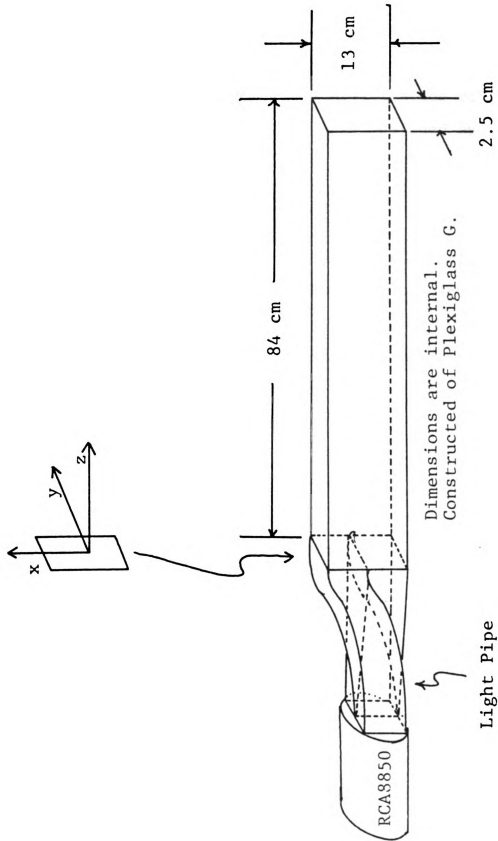


Figure 13. A large neutron time-of-flight detector.

To estimate the light loss as the position viewed down the cell is increased, the program listing in Appendix D was used. It assumes an extinction coefficient for the plexiglass of 0.005 cm^{-1} . The excitation coefficient $W=1/\lambda$, where λ is the attenuation length defined by the relation

$$(25) \quad \frac{I}{I_0} = \exp \left[-\frac{\ell}{\lambda} \right],$$

where I and I_0 are the transmitted and incident intensities, and λ is the path length. The loss at each plexiglass-air interface was assumed to be 5%, and the attenuation length of the liquid to be 3.3 meters. The program traces rays that are emitted at less than the critical angle of 41° and counts their losses as they travel down the length of the cell.

The fraction of the light transmitted versus the source position viewed is listed in Table 7. It is evident that the transmission is independent of X and Y but depends strongly on Z . Over the whole length of the detector one could expect to collect only 34% of the light emitted within the solid angle in which there is total internal reflection. Since, in order to increase the timing resolution, it is necessary to view the cell with a photomultiplier at each end, the PSD signal can be obtained from the photomultiplier that looks at a distance of one half the detector or less. In this case there is a predicted attenuation of 50%. The figure of merit M should then be decreased by a factor of $\sqrt{5}$. Thus, for NE224 the best figure of merit of 1.23 for

an equivalent electron energy of .62 to 1.24 MeV is now reduced to 0.87. This is already a poor figure of merit. The attenuation through the light pipe has to be taken into account also.

To measure the attenuation through the light pipe a 1.1 cm x 2.5 cm x 12.7 cm scintillation cell was constructed of plexiglass G and filled with NE224. The scintillator was then coupled to an Amperex 58AVP photomultiplier²¹ placed as shown in Figure 14. The block diagram of the electronics is shown in Figure 15. The photomultiplier was coupled to an Ortec 269 tube base. The linear dynode signal was amplified by an Ortec 113 preamplifier and further amplified and shaped by an Ortec 460 delay line amplifier. The singly differentiated output pulse was fed to a Canberra Model 8100 Multichannel analyzer.

The high voltage supply for the photomultiplier was set at 2240 volts. The coarse gain on the Ortec 460 was set at 50 with a fine gain of 1. Shaping time was set at 0.04 μ secs. A spectrum was collected for the Compton edge of a ²²⁸Th source collimated to irradiate the center 5/8 inches of the scintillator. The spectrum is shown in Figure 16a. The scintillator was then coupled to the light pipe and the light pipe coupled to the center of the 58AVP photomultiplier. It was necessary to readjust the gain of the Ortec 460 delay line amplifier to a coarse gain of 200. All other settings were kept unchanged. A new spectrum was collected of the ²²⁸Th Compton edge while irradiating the entire scintillator.

Table 7. Theoretical Light Transmission, in percent, through a Rectangular Scintillator of Dimension 2.7 cm x 83.8 cm x 12.8 cm. The source positions X, Y and Z are Defined in Figure 13.

Z = 83.8 cm				
	<u>Y = 0.0 cm</u>	<u>.33 cm</u>	<u>.67 cm</u>	<u>1.0 cm</u>
X = 0.0 cm	34.0	34.0	34.0	34.0
1.6 cm	34.0	34.0	34.0	34.0
3.2 cm	33.9	34.0	34.0	34.0
4.8 cm	33.9	33.9	33.9	33.9
Z = 62.9 cm				
	<u>Y = 0.0 cm</u>	<u>.33 cm</u>	<u>.67 cm</u>	<u>1.0 cm</u>
X = 0.0 cm	40.7	40.7	40.7	40.7
1.6 cm	40.7	40.7	40.7	40.7
3.2 cm	40.7	40.7	40.6	40.7
4.8 cm	40.6	40.6	40.6	40.6
Z = 41.9 cm				
	<u>Y = 0.0 cm</u>	<u>.33 cm</u>	<u>.67 cm</u>	<u>1.0 cm</u>
X = 0.0 cm	49.3	49.2	49.2	49.3
1.6 cm	49.2	49.2	49.2	49.2
3.2 cm	49.2	49.2	49.2	49.2
4.8 cm	49.1	49.1	49.1	49.1
Z = 21.0 cm				
	<u>Y = 0.0 cm</u>	<u>.33 cm</u>	<u>.67 cm</u>	<u>1.0 cm</u>
X = 0.0 cm	60.4	60.4	60.4	60.4
1.6 cm	60.4	60.4	60.4	60.3
3.2 cm	60.3	60.3	60.3	60.3
4.8 cm	60.2	60.2	60.2	60.1

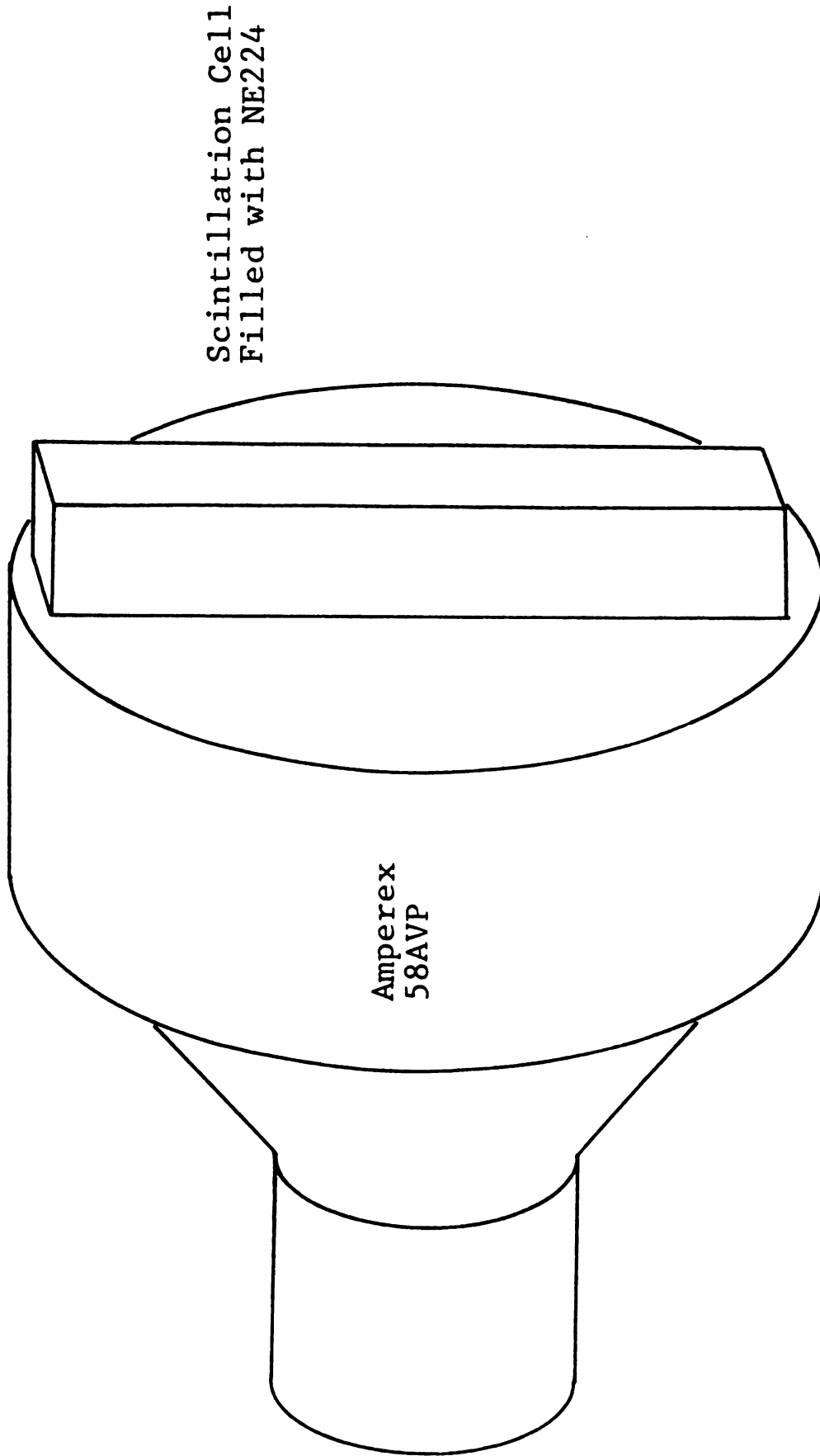


Figure 14. Placement of scintillation cell.

S c i n t i l l a t o r

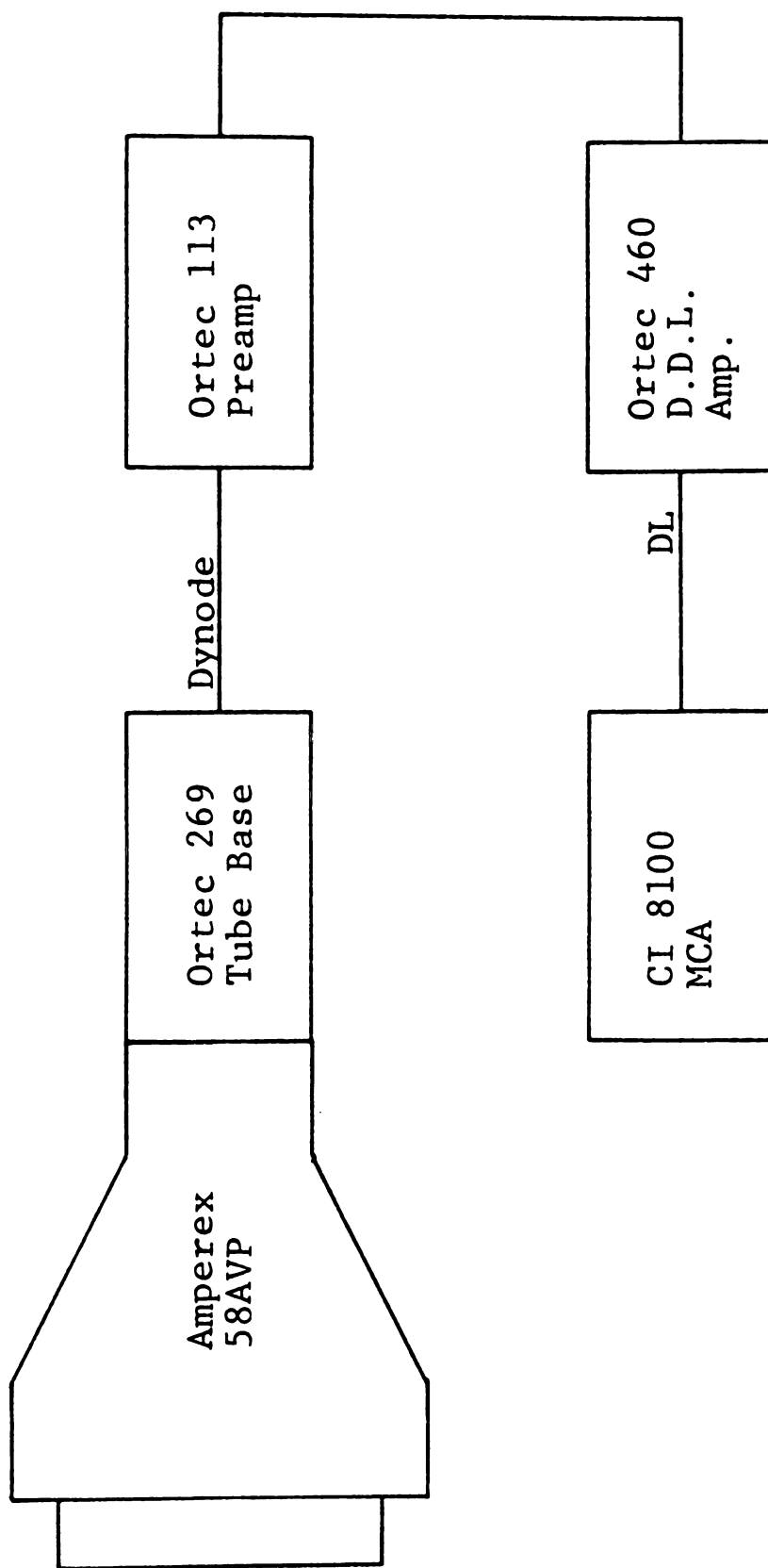


Figure 15. Electronic for measuring light pipe attenuation



Figure 16. Compton edge spectra without light pipe (a), and with light pipe (b)

This was done so that the entire light pipe would be utilized. However, the active area of the photomultiplier's photocathode utilized remained the same due to the reduction in area by the light pipe. This ensured that any change in the channel number of the Compton edge would not be due to the differing sensitivity of the center and the outer edge of the photocathode. The spectrum is shown in Figure 16b. Notice that the Compton edge has deteriorated due to the reduction in light collected.

Using the gain settings and channel numbers of the ^{228}Th Compton edge, an attenuation through the light pipe of approximately a factor of 6.3 is obtained. This would reduce the figure of merit by a factor of 2.5. This, coupled with the attenuation through the original neutron time-of-flight detector, would give a figure of merit of .35 for an equivalent electron energy range of .62 to 1.24 MeV for scintillations at the center of the detector. It is then clear that the light pipe, in this particular case, is the major source of degradation of the figure of merit.

5. DEOXYGENATION OF SCINTILLATION COUNTERS

5.1. Method of Deoxygenation

It is necessary to remove as much dissolved oxygen from the liquid scintillator as is possible, since the presence of oxygen leads to quenching of the desired triplet states. The method employed by this author was to place a long, thin teflon tube down to the base of the scintillation cell and bubble helium gas up through the liquid scintillator. The bubble stream mixes the liquid and allows for greater efficiency in removing the dissolved oxygen. It is also necessary to provide a means for the helium gas to escape. The excess helium was allowed to pass through a narrow constriction. This was done to prevent backstreaming of oxygen where it could interact with the surface of the scintillator liquid. Helium was chosen since this is an inert gas that does not quench the triplet states.

5.2. Diffusion Model

If the helium was not bubbled through the scintillator, but only allowed to interact with the open surface area, the removal of oxygen would require a much longer time period.

To show this, assume we have an $L=1$ meter long, cylindrical cell with one end open. If the scintillator has

an initial concentration of oxygen of K , and one end is then placed in contact with an oxygen free environment, the time for 95% of the oxygen to diffuse out of solution can be estimated by the following analysis: For diffusion in one direction only, ensured by the glass walls, the rate of flow of oxygen dQ/dt , through an area $dydz$, will depend on the rate of change of concentration dC/dx , times the area normal to x $dydz$, times a constant coefficient Δ , which has units of cm^2t^{-1} . Since dQ/dt is in the direction of decreasing concentration, we have

$$(26) \quad \frac{dQ}{dt} = - \Delta \left[\frac{dC}{dx} \right] dydz \quad ,$$

or for a rate of change of concentration

$$(27) \quad \frac{\partial C(x,t)}{\partial t} = \Delta \frac{\partial^2 C(x,t)}{\partial x^2} \quad .$$

With one end of the cell closed and the other exposed to a zero concentration of oxygen we have the initial conditions

$$(28) \quad C(0,t) = 0, \quad \frac{\partial C(L,t)}{\partial x} = 0, \quad C(x,0) = K.$$

Separation of variables leads to

$$(29) \quad X''(x) + \lambda X(x) = 0, \quad X'(L) = 0, \quad X(x) = K, \quad X(0) = 0 \quad \text{and}$$

$$(30) \quad T'(t) = -\lambda \Delta T(t), \quad \text{where } C(x,t) = X(x)T(t).$$

For Equation 29 we have a series of solution

$$(31) \quad X_n = A_n \sin(x\sqrt{\lambda}) + B_n \cos(x\sqrt{\lambda}).$$

For the boundry condition $X'(L)=0$ we have

$$(32) \quad X'(L) = A_n \sqrt{\lambda} \cos(L\sqrt{\lambda}) - B_n \sqrt{\lambda} \sin(L\sqrt{\lambda}) = 0,$$

and for $X(0)=0$

$$(33) \quad X_n(0) = B_n = 0, \text{ i.e. } \lambda = \left[\frac{2n-1}{2} \right]^2 \left[\frac{\pi}{L} \right]^2.$$

Thus,

$$(34) \quad X_n = A_n \sin \left[\frac{x\pi}{L} \left[\frac{2n-1}{2} \right] \right].$$

For Equation 30 we then get the solution

$$(35) \quad T_n(t) = C_n \exp \left[- \left[\frac{2n-1}{2} \right]^2 \Delta \left[\frac{\pi}{L} \right]^2 t \right],$$

which leads to a solution of Equation 27 of the form

$$(36) \quad C(x,t) = \sum_{n=1}^{\infty} A_n \exp \left[- \frac{\pi^2 \Delta t}{L^2} \left[\frac{2n-1}{2} \right]^2 \right] \sin \left[\frac{x\pi}{L} \left[\frac{2n-1}{2} \right] \right].$$

where

$$(37) \quad C(x,0) = K = \sum_{n=1}^{\infty} A_n \sin \left[\frac{x\pi}{L} \left[\frac{2n-1}{2} \right] \right].$$

Solving for A_n we get

$$(38) \quad A_n = \frac{K \int_0^L \sin \left[\frac{x\pi}{L} \left[\frac{2n-1}{2} \right] \right] dx}{\int_0^L \sin^2 \left[\frac{x\pi}{L} \left[\frac{2n-1}{2} \right] \right] dx} .$$

Integrating yields

$$(39) \quad A_n = \frac{4K}{\pi(2n-1)} .$$

The final solution is then

$$(40) \quad C = \frac{4K}{\pi} \sum_{n=1}^{\infty} \frac{\sin \left[\frac{x\pi}{L} \left[\frac{2n-1}{2} \right] \right] \exp \left[- \frac{\pi^2 \Delta t}{L^2} \left[\frac{2n-1}{2} \right]^2 \right]}{(2n-1)} .$$

$$(41) \quad \bar{C} = \frac{\int_0^L C(x,t) dx}{L} = \frac{8K}{\pi^2} \sum_{n=1}^{\infty} \frac{\exp \left[- \frac{\pi^2 \Delta t}{L^2} \left[\frac{2n-1}{2} \right]^2 \right]}{(2n-1)} .$$

Solving for $\bar{C}(t=?) = .05K$ we can neglect $n=2,3,\dots$ terms since they are much less than the $n=1$ term for the above condition. Thus,

$$(42) \quad t = \frac{4L^2}{\Delta \pi^2} \log_e \left[\frac{8}{\pi^2 (0.05)} \right] .$$

The constant of diffusivity Δ for NE213 is assumed to be on the order of that for cyclohexane which has a diffusivity for oxygen at 20°C of $4 \times 10^{-5} \text{ cm}^2 \text{ sec}^{-1}$.²² This gives us the time t , at which 95% of the oxygen is removed, of 2.8×10^8 seconds, or approximately 9 years.

It is therefore imperative that the inert gas be bubbled through the liquid to provide thorough mixing. In this way a large gradient of concentration exists at the gas-liquid interface speeding the removal of oxygen.

6. A NEUTRON TIME-OF-FLIGHT DETECTOR WITH IMPROVED PULSE SHAPE DISCRIMINATION

6.1. The Detector

A 45 mm diameter pyrex glass cylinder 1.24 meters long was constructed as shown in Figure E1. The windows on the end are flat pyrex. An RCA 8850 photomultiplier was coupled to one end. The 45 mm diameter of the cell made it unnecessary to use a light pipe to couple the photomultiplier to the cell. This improves the light collection efficiency. The attenuation of light down the detector while it contained NE213 was measured by the methods described in Appendix E. The attenuation length for the detector filled with NE213 was equal to $0.95 \pm .01$ meters. Thus, the attenuation A for the detector as a function of the position x of the scintillation from the photomultiplier can be expressed

$$(43) \quad A = 1 - \exp\left[-\frac{x}{0.95}\right] .$$

If one were willing to accept a reduction in the figure of merit of a factor of 1.4, then the farthest a scintillation could occur from the photomultiplier would be $x = .66$ meters. This is over half the length of the detector. Since, for neutron time-of-flight studies, one uses a photomultiplier

at each end for reasons of time resolution, a photomultiplier is always close enough for good pulse shape discrimination.

6.2. Performance

The pulse shape discrimination characteristics of the detector were measured for both NE213 and NE224 as the active scintillator.

6.2.1. Detector Filled with NE213

A test of the figure of merit obtainable from the scintillator for NE213 was made for a source position near the photomultiplier and for a position midway down the detector. This was accomplished by placing the appropriate source at the two positions along the detector. The figure of merit at these two positions were obtained as a function of electron equivalent energy deposited in the scintillator.

The electronics used are those in Figure 3. The data were collected on the PDP 11/45. The same procedures were used to tune the electronics as earlier. First a spectrum of the 1.33 MeV ^{60}Co Compton edge was taken for a position near the photomultiplier. Then the ^{60}Co source was replaced with a PuBe source and a spectrum taken of the pulse shape discrimination signal, gated as a function of energy. The results are tabulated in Table 8. Representative plots of the data are in Figure 17. The procedure was then repeated for a position at the center of the detector. The results are given in Table 9 and spectra shown in Figure 18.

Table 8. Figure of Merit (M) for a 1.24 m x 45 mm NE213 Scintillator with Source at Near End of Scintillator.

Energy Range [MeV]	Figure of Merit
1.1 thru 5.1	1.2
3.6 thru 5.1	1.3
2.4 thru 5.1	1.0
1.7 thru 2.4	1.3
1.1 thru 1.7	1.2
.62 thru 1.1	1.0
.25 thru .38	.85

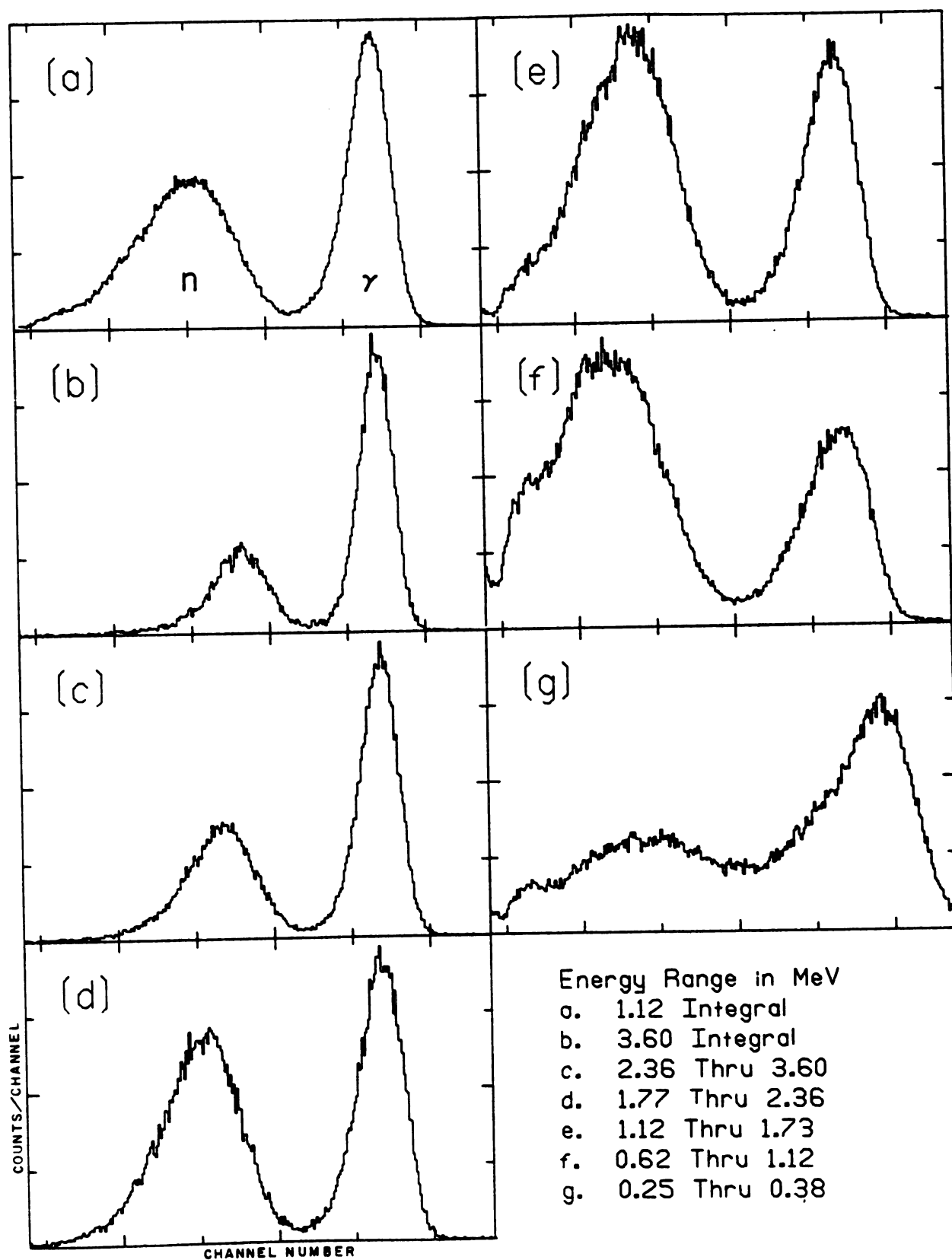


Figure 17. P.S.D. for NE213 cell 1.24 m, near end.

Table 9. Figure of Merit (M) for a 1.24 m x 45 m NE213 Scintillator with Source at Center of Scintillator.

Energy Range [MeV]	Figure of Merit
1.02 Integral	.98
3.29 Integral	1.00
2.16 thru 3.29	.99
1.58 thru 2.16	1.0
1.02 thru 1.58	.95
.56 thru 1.02	.90
.45 thru .67	.80

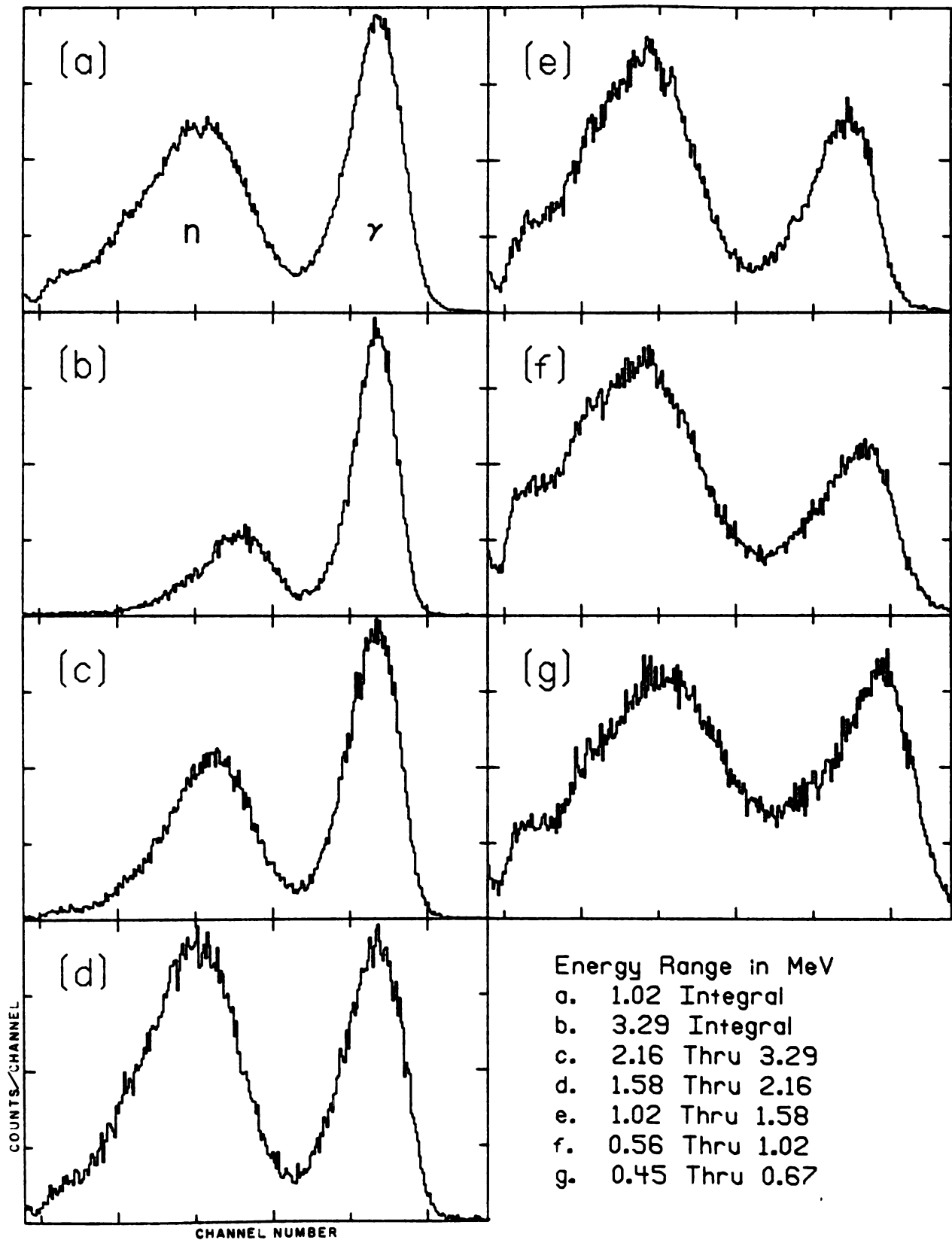


Figure 18. P.S.D. for NE213 cell 1.24 m, middle.

When the Compton edge channel numbers for the two positions were used to evaluate the attenuation one finds that the figure of merit should deteriorate in the central position by a factor of 1.37. For an electron equivalent energy range of 3.6 to 4.4 MeV the observed degradation of the figure of merit was a factor of 1.35. It therefore appears that the reduction in the figure of merit is due mainly to light loss and not time spread due to multiple paths of transit of the light. If this were the case one would expect the figure of merit to be worse than that predicted by light attenuation alone.

6.2.2. Detector refilled with NE224

The detector was emptied of the NE213, refilled NE224, which was then deoxygenated. The pulse shape discrimination performance of the detector was evaluated using the same procedure. The results are tabulated in Tables 10 and 11. Typical spectra are shown in Figures 19 and 20. As before, the PSD quality of NE224 is inferior to that of NE213. However, the ability of NE224 to be contained in a plexiglass container makes it useful in some instances where the pulse shape discrimination characteristics are not of prime importance.

6.3. Comments

As shown in Appendix E, the light transmission down a detector decreases as the diameter of the detector decreases. Therefore, if a narrow detector is made to achieve high time

resolution, the figure of merit deteriorates due to the increased light loss.

Table 10. Figure of Merit for a 1.24 m x 45 mm NE224 Scintillator with Source at Near End of Scintillator.

Energy Range (M)	Figure of Merit
1.14 thru 5.07	.98
3.65 thru 5.07	1.15
2.39 thru 3.65	1.10
1.76 thru 2.39	1.08
1.14 thru 1.76	1.01
.63 thru .94	.97
.25 thru .38	.85

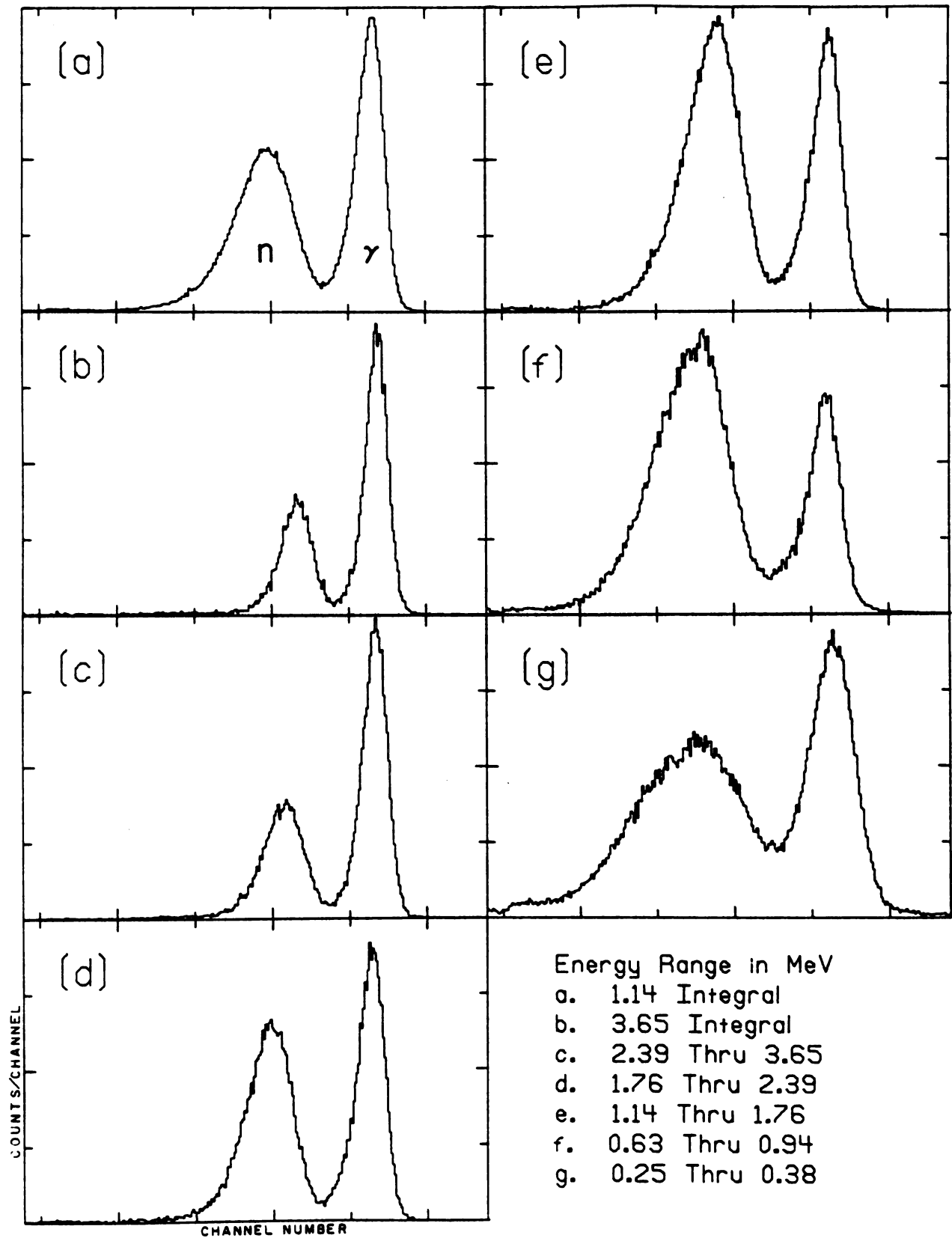


Figure 19. P.S.D. for NE224 cell 1.24 m. near end.

Table 11. Figure of Merit for 1.24 m x 45 mm Scintillator filled with NE224 with Source at Center of Scintillator.

Energy Range (M)	Figure of Merit
1.12 Integral	.85
3.57 Integral	.93
2.34 thru 3.57	.93
1.73 thru 2.34	.92
1.12 thru 1.73	.88
.61 thru .91	.86
.46 thru .69	.82

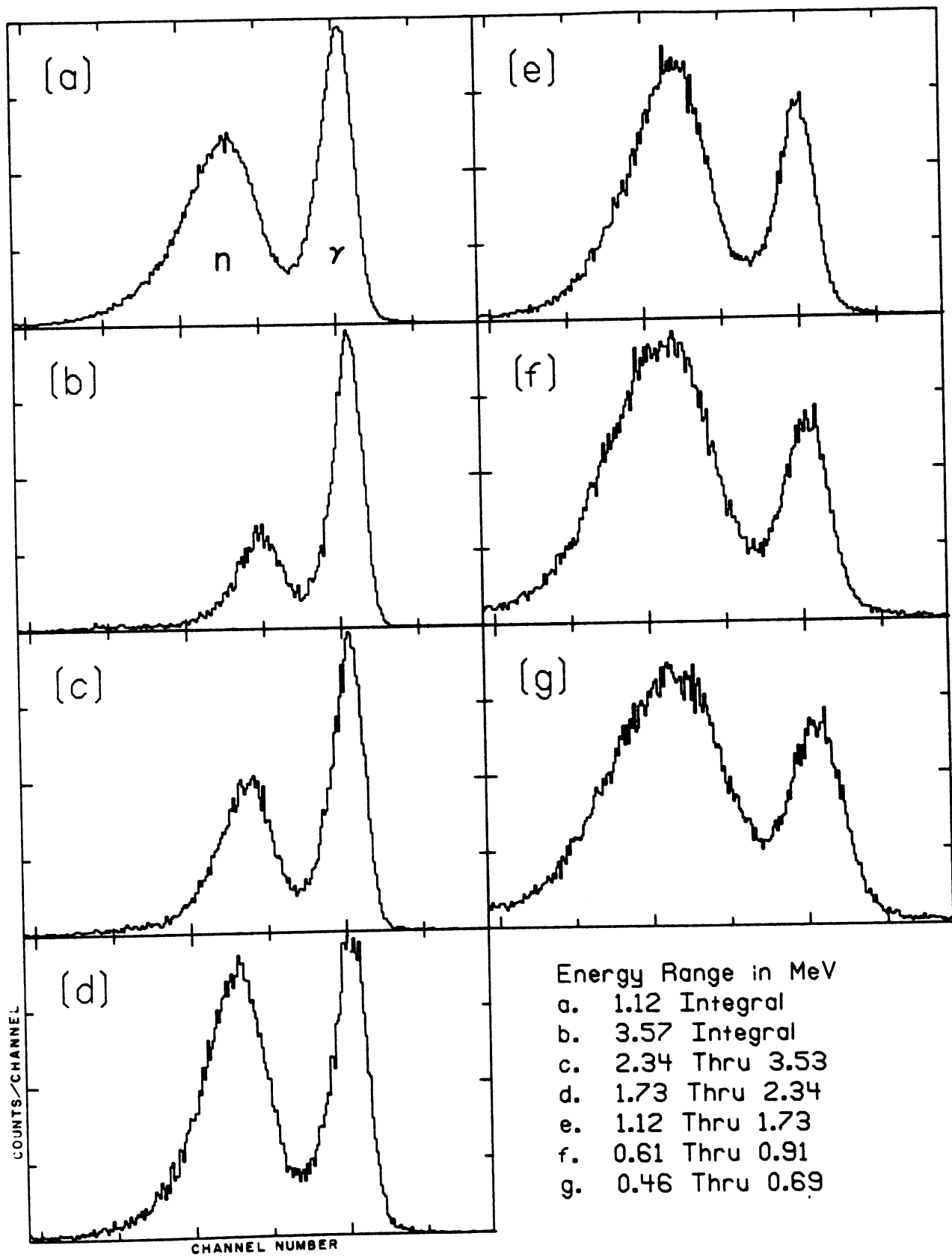


Figure 20. P.S.D. for NE224 cell 1.24 m. middle.

7. Photomultiplier Problems

7.1. Gas Ionization

A photomultiplier, after having produced photoelectrons in response to incoming photons, may produce an after-pulse.^{2 3} The photomultiplier contains some residual gas and as the first group of electrons is emitted from the photocathode and accelerated towards the first dynode the electrons ionize the residual gas. These positive ions are then accelerated back towards the photocathode, whereupon they liberate more electrons. This after-pulse occurs, of course, after the main pulse. The time at which it occurs depends on the kind of residual gas and the accelerating potential. If the after pulses occur soon enough they can interfere with the desired signal.

7.2. After-Pulses in the Present System

Afterpulses were observed in taking data with the small detector, shown in Figure 8, while it was filled with NE213. These after-pulses occurred typically 700 nsecs later. The anode pulse with its associated after-pulse is shown in Figure 21a. Also shown in Figures 21b and 21c are the dynode pulses after delay line shaping, and double delay line shaping. Since the zero-crossover method of pulse shape discrimination depends on the time the double delay line

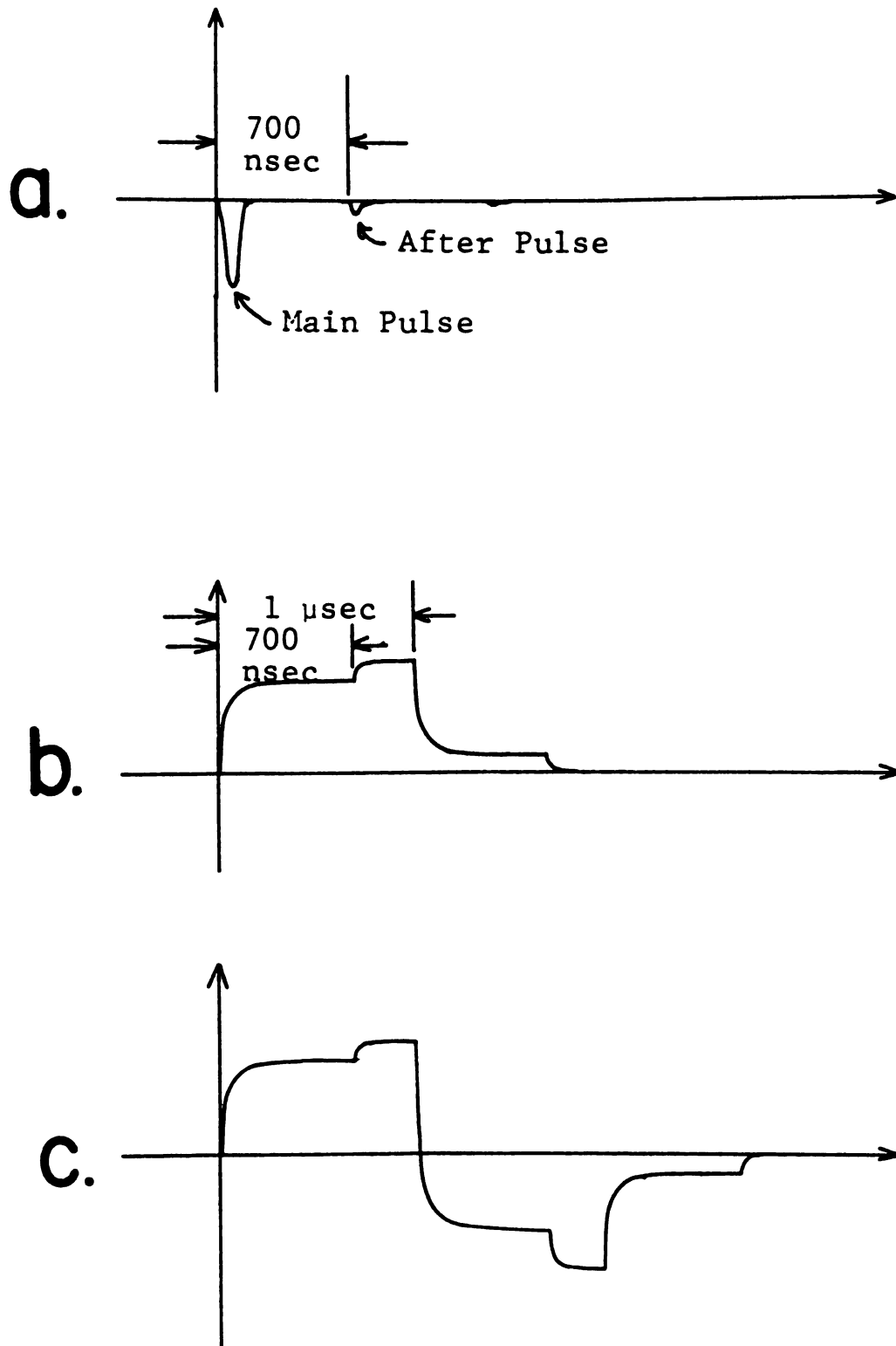


Figure 21. After-pulses in anode signal (a), singly differentiated dynode signal (b), and doubly differentiated dynode signal (c) with 1 μ sec delay line shaping.

shaped pulse crosses zero, it is clear that the after-pulse would affect the pulse shape discrimination ability of the system. One method of eliminating afterpulses is to age the tube as suggested by Kuchnir and Lynch.²⁴

The method employed here was to process the signal before the after pulse occurred. This was accomplished by replacing the 1 μ sec delay lines in the Canberra delay line amplifier with 400 nsecs delay lines. The effect of this can be seen by noting the delay line and double delay line shaped signals in Figures 22a and b.

The effect on the figure of merit was measured by first accumulating the PSD spectra for NE213 in the small cell of Figure 8, using the electronics in Figure 3. The delay line amplifier was unmodified. This was done for a discrimination level of .5 to 5.5 MeV equivalent electron energy. The delay line amplifier was then replaced with a modified delay line amplifier and a new spectrum taken. The results are shown in Table 12. The observed pulse shape spectra are shown in Figures 23a and b respectively. The increase of figure of merit from .95 to 1.28 represents a significant increase. To achieve the same goal by increased light collection would necessitate an increase of photons collected by a factor of 1.8.

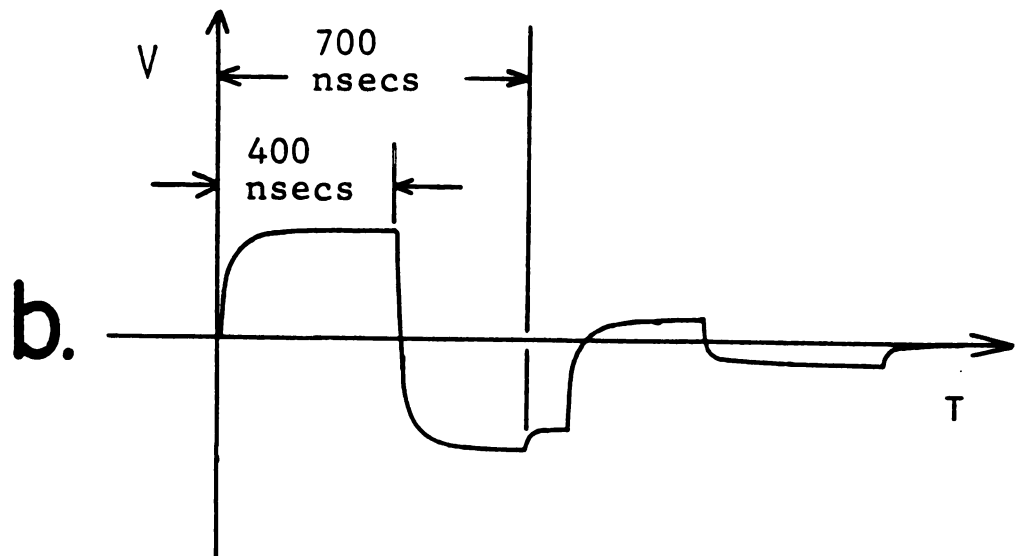
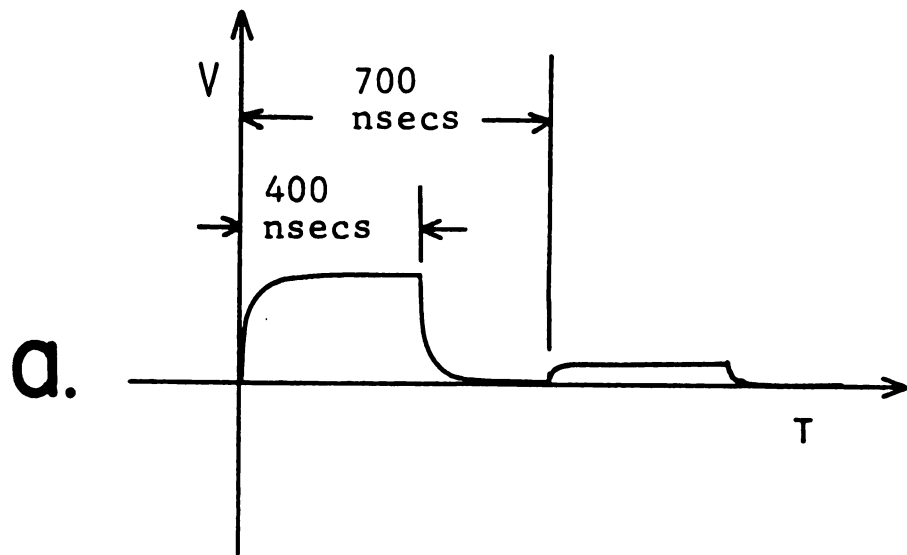


Figure 22. After-pulses in singly differentiated dynode signal (a) and doubly differentiated dynode signal (b) with 400 nsecs delay line shaping.



Figure 23. PSD spectra with 1 μ sec double delay line shaping (a), PSD spectra with 400 nsecs double delay line shaping.

Table 12. Figure of Merit for 1.0 μ sec Double Delay Line Shaping and 400 nsecs Double Delay Line Shaping with PuBe Source.

Discrimination Level at 500 KeV	
1.0 μ sec Shaping	400 nsecs Shaping
M = 0.95	M = 1.28

8. CONCLUSION

Building a neutron time-of-flight detector having good pulse shape discrimination requires that attention be paid to optimizing the collection of the light from the radiation induced scintillation. This is done by maintaining the largest diameter one can tolerate in the detector while still maintaining good timing resolution. Also, elimination of light pipes, or minimizing the reduction in area through the light pipe, is of major benefit in eliminating light loss. Light loss through attenuation in the scintillator itself is of minor importance except for very large detectors.

Deoxygenation of the scintillator must be done with care to prevent recontamination with atmospheric oxygen. It has been shown that in bubbling the inert gas through the scintillator it is necessary to provide a bubble stream so as to mix the scintillator and thus reduce the time necessary to deoxygenate the scintillator.

After-pulses can be a major source of degradation in the figure of merit and can easily be eliminated as a source of problems by simply changing the double delay line shaping time.

Amplifier noise should be reduced so as to provide good pulse shape discrimination at the low energy end of the range detected.

By considering these factors a neutron time-of-flight detector can be built with acceptable neutron/gamma-ray pulse shape discrimination. NE213 appears to be the optimal choice for detector geometries not requiring construction with plexiglass.

APPENDICES

APPENDIX A

COMPUTER PROGRAM FOR CALCULATING \bar{t} , D and ϵ

APPENDIX A

COMPUTER PROGRAM FOR CALCULATING $\bar{\epsilon}$, D and ϵ

```
DO 2 R=500.00,6000.0,500.0
N=R/2
AF=.8
AS=.2
TF=4.0
TS=25.0
CALL PSD(AF,AS,TF,TS,R,N,DVE,TME)
AF=.5
AS=.5
TS=47.0
CALL PSD(AF,AS,TF,TS,R,N,DVP,TMP)
D=(TMP-TME)/SQRT(DVP**2+DVE**2)
PRINT 1,D
1 FORMAT (' D=',F6.2)
2 CONTINUE
END
```

```

SUBROUTINE PSD(AF,AS,TF,TS,R,N,DV,TM)
WN=0
T=0
TM=0
TM2=0
2 T=T+.1
EXF=0
IF((T/TF).LE.170.0) EXF=EXP(-T/TF)
EXS=0
IF((T/TS).LE.170.0) EXS=EXP(-T/TS)
F=AF*(1-EXF)+AS*(1-EXS)
FDT=AF/TF*EXF+AS/TS*EXS
AL=0
IF((F.NE.0.0).AND.(F.NE.1.0).AND.(FDT.NE.0.0))
1AL=(R-N)*ALOG(1.0-F)+(N-1)*ALOG(F)+ALOG(FDT)+R*.69
PT=0
IF((AL.GE.-170.0).AND.(AL.NE.0.0)) PT=EXP(AL)
WN=WN+PT*.5
TM=TM+T*PT*.5
TM2=TM2+T**2*PT*.5
IF(T.LE.1000) GO TO 2
TM=TM/WN
TM2=TM2/WN
DV=SQRT(TM2-TM**2)
PRINT 3,DV,TM
3 FORMAT (' STD DEV=',F6.2,' T=',F6.2)
RETURN
END

```

APPENDIX B

COMPUTER PROGRAM FOR GENERATING PULSE SHAPE SIGNATURES

APPENDIX B

COMPUTER PROGRAM FOR GENERATING PULSE SHAPE SIGNATURES

```
DIMENSION DY(256),DX(256)
DO 4 K=1,7
R=25.*1.9307**K
N=R/2
YMAX=0.
DO 1 I=1,256
T=2.+8./255.*(I-1)
DX(I)=T
DY(I)=PT(.8,.2,4.,25.,R,N,T)+PT(.5,.5,4.,47.,R,N,T)
1 IF(DY(I).GE.YMAX) YMAX=DY(I)
DO 2 I=1,256
DY(I)=DY(I)/YMAX
C UNIT 106 IS A FILE FOR TEMPORARY STORAGE OF PSD SIGNATURE
C UNIT 106 IS THEN CALLED BY DRAFTRESIST TO BE PLOTTED
2 WRITE(106,3) DX(I),DY(I)
3 FORMAT(10X,2F10.3)
4 WRITE(106,5)
5 FORMAT('END')
END
```

APPENDIX B

```
      FUNCTION PT(AF,AS,TF,TS,R,N,T)
40     EXF=0.0
50     IF((T/TF).LE.170.0) EXF=EXP(-T/TF)
60     EXS=0
70     IF ((T/TS).LE.170.0) EXS=EXP(-T/TS)
80     F=AF*(1-EXF) +AS*(1-EXS)
90     FDT=AF/TF*EXF+AS/TS*EXS
100    AL=0
110    IF((F.NE.0.0).AND.(F.NE.1.0).AND.(FDT.NE.0.0))
120 1AL=(R-N)*ALOG(1.0-F)+(N-1)*ALOG(F)+ALOG(FDT)+R*0.69
130    PT=0
140    IF((AL.GE.-170.0).AND.(AL.NE.0.0)) PT=EXP(AL)
      RETURN
      END
```

APPENDIX C

COMPUTER PROGRAM FOR CALCULATING FIGURE OF MERIT D AS A
FUNCTION OF PULSE HEIGHT FRACTION K

APPENDIX C

COMPUTER PROGRAM FOR CALCULATING FIGURE OF MERIT D AS A
FUNCTION OF PULSE HEIGHT FRACTION K

```
R=300
DO 2 N=20,280,20
  AF=.8
  AS=.2
  TF=4.0
  TS=25.0
  CALL PSD(AF,AS,TF,TS,R,N,DVE,TME)
  AF=.5
  AS=.5
  TS=47.0
  CALL PSD(AF,AS,TF,TS,R,N,DVP,TMP)
  D=(TMP-TME)/SQRT(DVP**2+DVE**2)
  PRINT 1,D
1  FORMAT (' D=',F6.2)
2  CONTINUE
END
```

APPENDIX C

```

SUBROUTINE PSD(AF,AS,TF,TS,R,N,DV,TM)
WN=0
T=0
TM=0
TM2=0
2  T=T+0.1
   EXF=0
   IF ((T/TF).LE.170.0) EXF=EXP(-T/TF)
   EXS=0
   IF ((T/TS).LE.170.0) EXS=EXP(-T/TS)
   F=AF*(1-EXF)+AS*(1-EXS)
   FDT=AF/TF*EXF+AS/TS*EXS
   AL=0
   IF ((F.NE.0.0).AND.(F.NE.1.0).AND.(FDT.NE.0.0))
1  AL=(R-N)*ALOG(1.0-F)+(N-1)*ALOG(F)+ALOG(FDT)+R*0.69
   PT=0
   IF((AL.GE.-170.0).AND.(AL.NE.0.0)) PT=EXP(AL)
   WN=WN+PT*0.5
   TM=TM+T*PT*0.5
   TM2=TM2+T**2*PT*0.5
   IF (T.LE.1000) GO TO 2
   TM=TM/WN
   TM2=TM2/WN
   DV=SQRT(TM2-TM**2)
   PRINT 3,DV,TM
3  FORMAT (' STD DEV=',F6.2,' T=',F6.2)
   RETURN
END

```

APPENDIX D

COMPUTER PROGRAM FOR CALCULATING LIGHT ATTENUATION IN
A RECTANGULAR DETECTOR

APPENDIX D

COMPUTER PROGRAM FOR CALCULATING LIGHT ATTENUATION IN A RECTANGULAR DETECTOR

```

COMMON X0,Y0,Z0,THETA,PHI,L,w,h,FRAC,D,EXTNK,SCAT
REAL*4 X0,Y0,Z0,THETA,PHI,L,w,h,FRAC,D,EXTNK,TRNS(10)
DATA PI/3.141592654/
w=2.67
h=12.83
L=83.83
D=0.1588
SCAT=.95
EXTNK=0.005
THI=PI/25.0
PHII=49.0/50.0/180.0*PI
DO 7 J3=1,4
PRINT 5
5  FORMAT (' ')
DO 4 J1=1,4
DO 6 J2=1,4
X=h/8.0*(J1-1)
Y=w/8.0*(J2-1)
Z=L/4.0*(J3-1)
    PHI=41.0/180.0*PI
TD=0.0
DO 2 I=1,50
    TH=0.0
DO 1 J=1,50
X0=X
Y0=Y
Z0=Z
THETA=TH
CALL LFRAC
TD=TD+FRAC*5.81/4.0/PI* $\cos(\text{PHI})$ *THI*PHII* $\exp(-0.003*L/\sin(\text{PHI}))$ 
1  TH=TH+THI
2  PHI=PHI+PHII
    TD=TD*100.0
6  TRNS(J2)=TD
4  PRINT 3,(TRNS(I1),I1=1,4)
3  FORMAT (' ',4F7.2)
7  PRINT 8
8  FORMAT(' ')
STOP
END

```

APPENDIX D

```

      SUBROUTINE LFRAC
      COMMON XO,YO,ZO,THETA,PHI,L,W,H,FRAC,D,EXTNK,SCAT
      REAL*4 XO,YO,ZO,THETA,PHI,L,W,H,FRAC,D,EXTNK,PI,W1,H1,R1,R2
      DATA PI/3.141592654/
      PHI=PI/2.0-PHI
      FRAC=1.0
1   H1=H/2.0
      W1=W/2.0
      ST=SIN(THETA)
      CT=COS(THETA)
      SP=SIN(PHI)
      IF (CT*SP) 2,8,3
2   H1=-H/2.0
3   IF (ST*SP) 4,11,5
4   W1=-W1
5   R1=(H1-XO)/(SP*CT)
      R2=(W1-YO)/(SP*ST)
      IF(R1.GT.R2) GO TO 6
      XO=H1
      YO=R1*SP*ST+YO
      ZO=ZO+R1*COS(PHI)
      THETA=PI-THETA
      IF (THETA.LT.0.0) THETA=THETA+2*PI
      IF(ZO.GE.L) GO TO 12
      FRAC=FRAC*EXP(-2.0*D/ABS(SP*CT)*EXTNK)*SCAT
      GO TO 7
6   XO=R2*SP*CT+XO
      YO=W1
      ZO=ZO+R2*COS(PHI)
      THETA=2.0*PI-THETA
      IF(ZO.GE.L) GO TO 12
      FRAC=FRAC*EXP(-2.0*D/ABS(SP*ST)*EXTNK)*SCAT
7   IF (ZO.GE.L) GO TO 12
      GO TO 1
8   IF (ST*SP) 9,10,10
9   W1=-W1
10  R1=(W1-YO)/(ST*SP)
      XO=0.0
      YO=W1
      ZO=ZO+R1*COS(PHI)
      THETA=2.0*PI-THETA
      IF(ZO.GE.L) GO TO 12
      FRAC=FRAC*EXP(-2.0*D/ABS(SP*ST)*EXTNK)*SCAT
      GO TO 7
11  R1=(H1-XO)/(CT*SP)
      YO=0.0
      XO=H1
      ZO=ZO+R1*COS(PHI)
      THETA=PI-THETA
      IF (THETA.LT.0.0) THETA=THETA+2.0*PI
      IF(ZO.GE.L) GO TO 12

```

78
APPENDIX D

```
FRAC=FRAC*EXP(-2.0*D/AES(SP*CT)*EXTLK)*SCAT  
GO TO 7  
12 PHI=PI/2.0-PHI  
RETURN  
END
```

APPENDIX E

LIGHT ATTENUATION IN LIQUID ORGANIC SCINTILLATORS

LIGHT ATTENUATION IN LIQUID ORGANIC SCINTILLATORS

John E. Yurkon and Aaron Galonsky

Cyclotron Laboratory, Michigan State University
East Lansing, Michigan, USA

Abstract

Measurements of the attenuation length of monochromatic light in NE 213 and NE 224 and of the wavelength-averaged attenuation length in NE 213 are given in order to provide the designer of large-volume detectors with information necessary in deciding how large a detector can be constructed without excessive loss of light. In particular, the attenuation length of scintillation light in NE 213 is found to be 2.16 ± 0.24 m.

*This material is based upon work supported by the National Science Foundation under Grant No. Phy-7822696.

E1. INTRODUCTION

The timing and neutron/gamma-ray pulse shape discrimination qualities of time-of-flight detectors depend in part on the collection efficiency of the light produced in a scintillation. Therefore, in building a large-volume detector it is important to know the light attenuation length λ_ℓ given by

$$(1) \quad I/I_0 = \exp\left(\frac{-d}{\lambda_\ell}\right)$$

where I_0 is the incident light intensity, I the transmitted light intensity, and d the length of the path traveled.

Two different methods of measuring the light attenuation lengths of the liquid scintillators^{2,3} NE 213 and NE 224 will be discussed.

E2. METHODS OF MEASUREMENT

E2.1. Direct

A collimated beam of light was directed down a 45 mm O.D. cylindrical Pyrex cell (Fig. E1) filled with the liquid scintillator. Placed inside of the cell was a mirror attached to a teflon cylinder. The teflon cylinder contained a piece of iron so that it could be moved along the length of the cell with an external magnet. The reflected light intensity was measured with a light meter. A photograph of the apparatus is shown in Fig. E2.

The reflected light intensities were measured for various positions of the mirror. Since the number of interfaces remained constant, the resultant plot of intensity versus path length in the liquid should reflect only the attenuation by the liquid scintillator.

The wavelength of maximum emission for NE 213 and NE 224 is 4250 \AA^{24} . Therefore, it is desirable to measure the light attenuation length near this wavelength. The 4416 \AA^0 line of a helium-cadmium laser was used as the closest available wavelength. To see if there is a wavelength dependence on the attenuation length, the 4689 \AA^0 line of a krypton laser was also used.

The data for NE 213 and NE 224 are shown in Figs. E3 and E4, respectively. The measured attenuation lengths obtained from a least-squares fit are listed in Table E1.

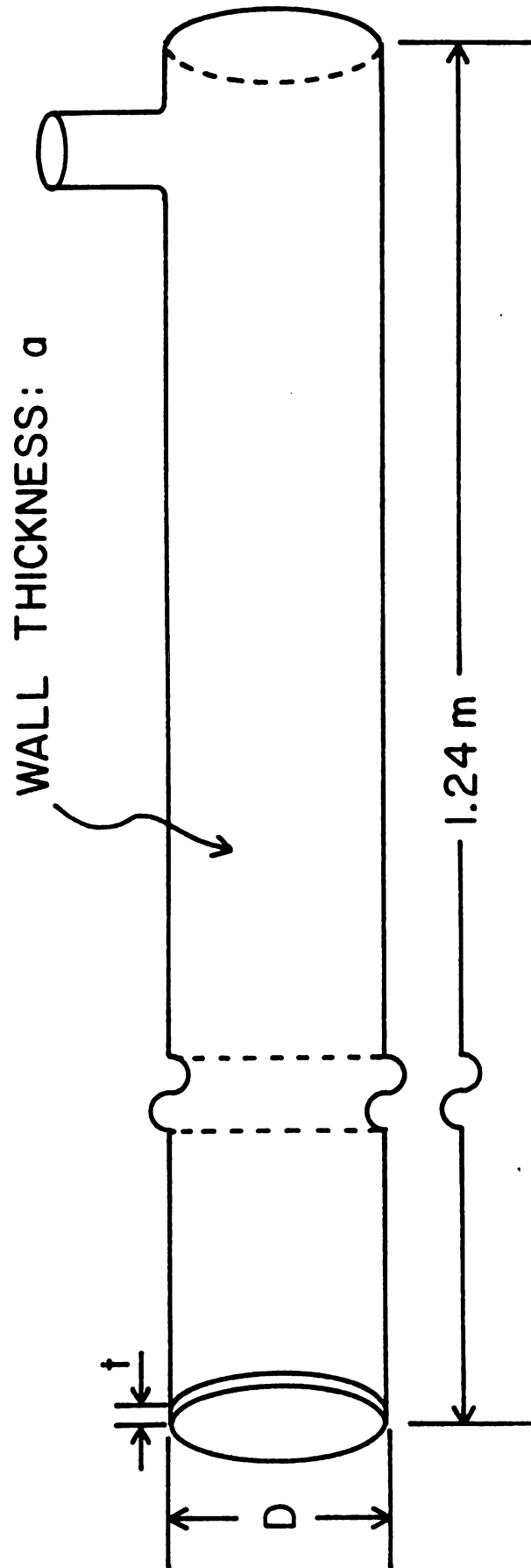


Figure E1. Details of scintillator cell with dimensions

D	a	t
$45 \pm 1 \text{ mm}$	$2.0 \pm 0.2 \text{ mm}$	2 mm
$22.0 \pm .6 \text{ mm}$	$1.5 \pm 0.2 \text{ mm}$	2 mm

constructed of Pyrex glass

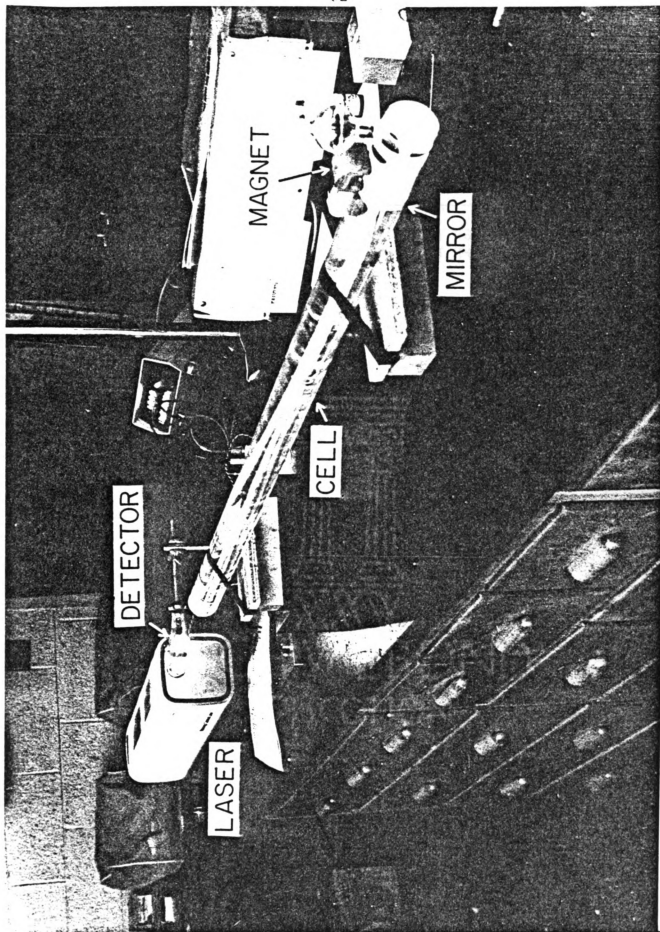


Figure E2. Photograph of scintillator cell and laser setup.

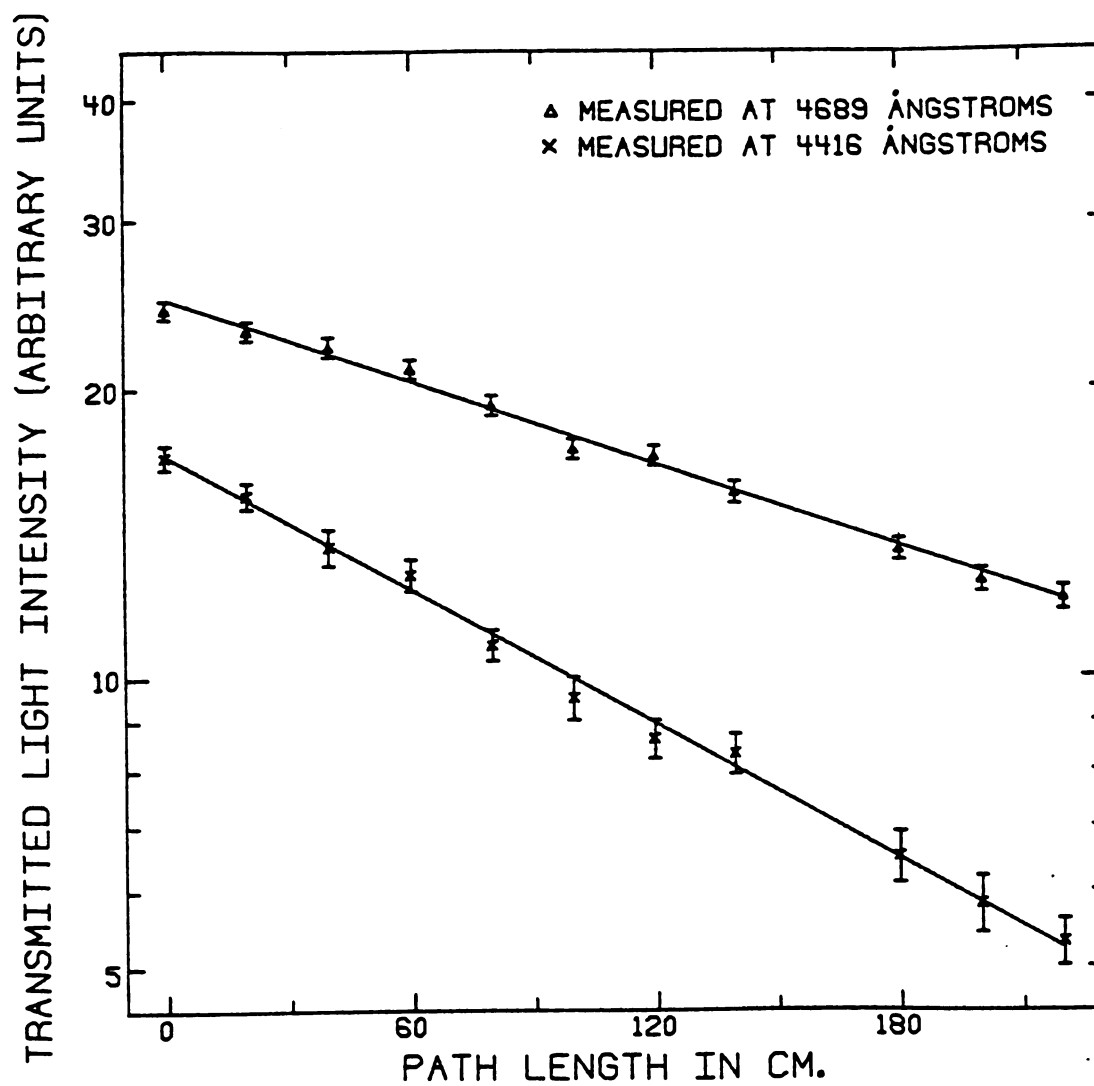


Figure E3. Transmitted light intensity vs. path length for NE213.

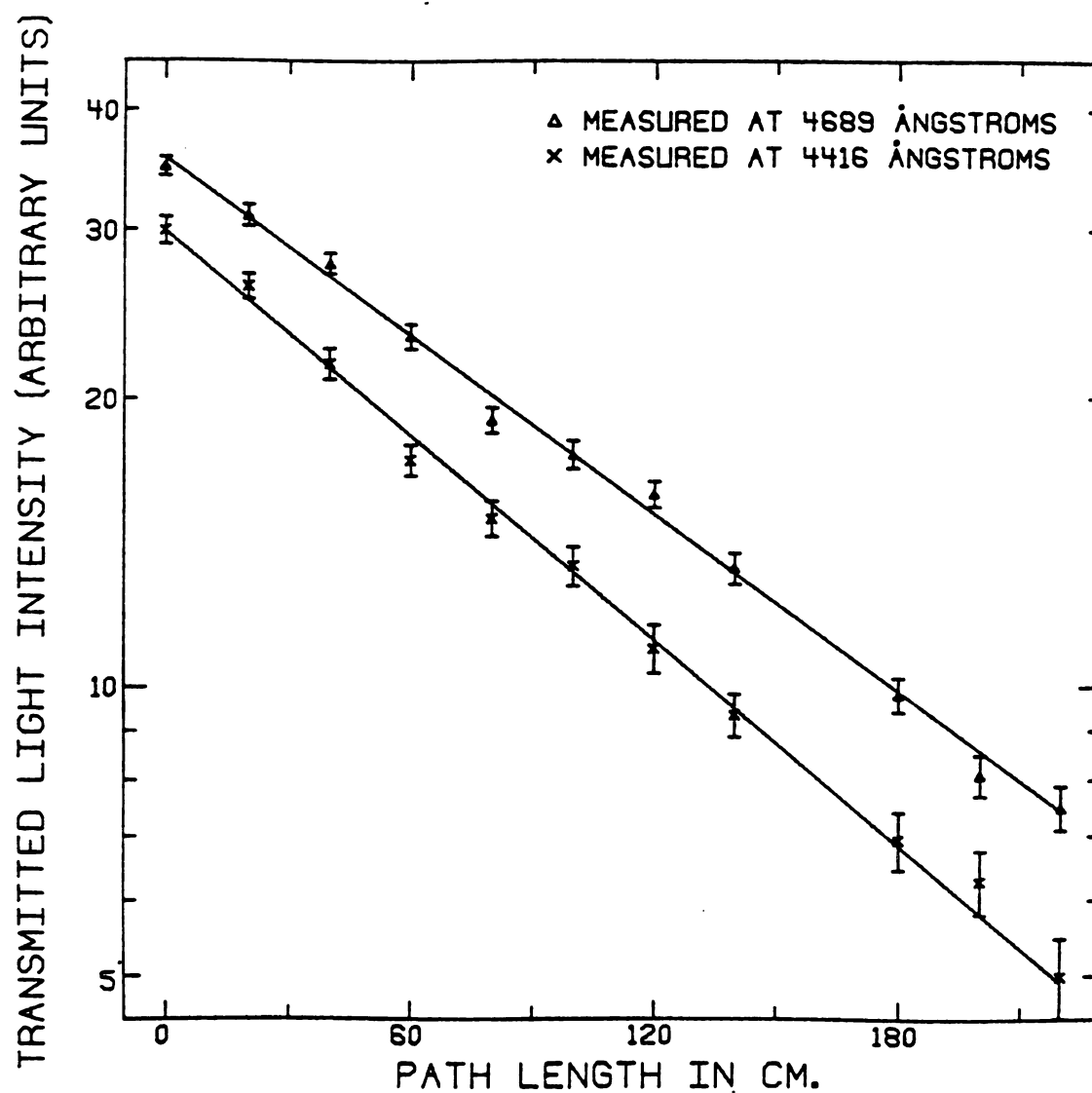


Figure E4. Transmitted light intensity vs. path length for NE224.

Table I. Attenuation lengths in meters as measured with laser light.

	4416 $\overset{\circ}{\text{\AA}}$	4689 $\overset{\circ}{\text{\AA}}$
NE 213	1.85 ± 0.07	3.02 ± 0.10
NE 224	1.22 ± 0.03	1.40 ± 0.03

As can be seen, the attenuation length is shorter for the wavelength closer to 4250 \AA . Furthermore, NE 213 exhibits a stronger wavelength dependence than NE 224.

E2.2. Measurement with Radiation-Induced Scintillations

A measurement of the wavelength-averaged attenuation length for NE 213 was made as a comparison to the laser method. The spectrum of radiation-induced scintillations in NE 213 does not consist of a single line. It has a finite width, probably on the order of a few hundred Angstroms. The attenuation length of NE 213 is wavelength dependent, as shown in Table E1. Thus, a filtering of the induced scintillations takes place with the result that the rate of attenuation decreases as the more rapidly attenuated wavelengths are removed. The wavelength-averaged attenuation length is obtained by picking a region of the data where the attenuation appears to be exponential.

The mirror was removed, and an RCA 8850 photomultiplier was attached to one end of the 45 mm O.D. cell. The cell was wrapped loosely with black paper so that the light was collected only by total internal reflection. A collimated Th-228 source was placed along the side of the cell as shown in Fig. E5. A block diagram of the electronics is shown in Fig. E6. The channel number of the Compton edge of the 2.62-MeV γ -ray was measured for various positions of the source.

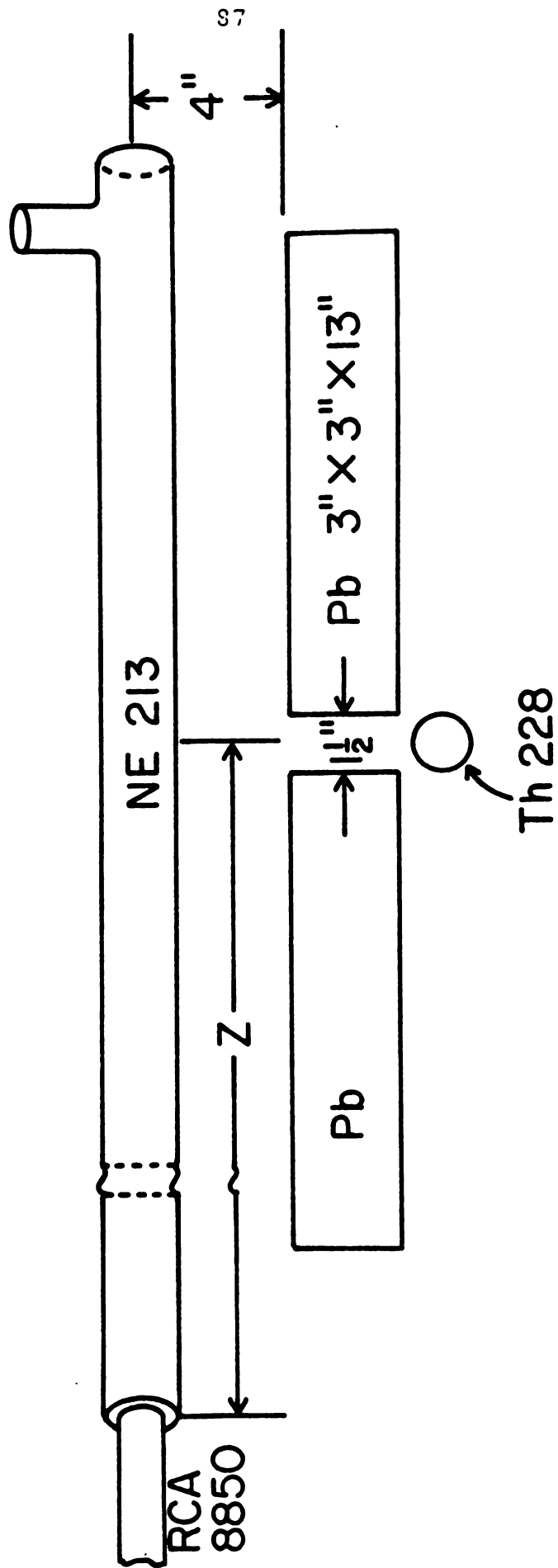


Figure E5. The setup for measurements of the "wavelength-averaged attenuation length".

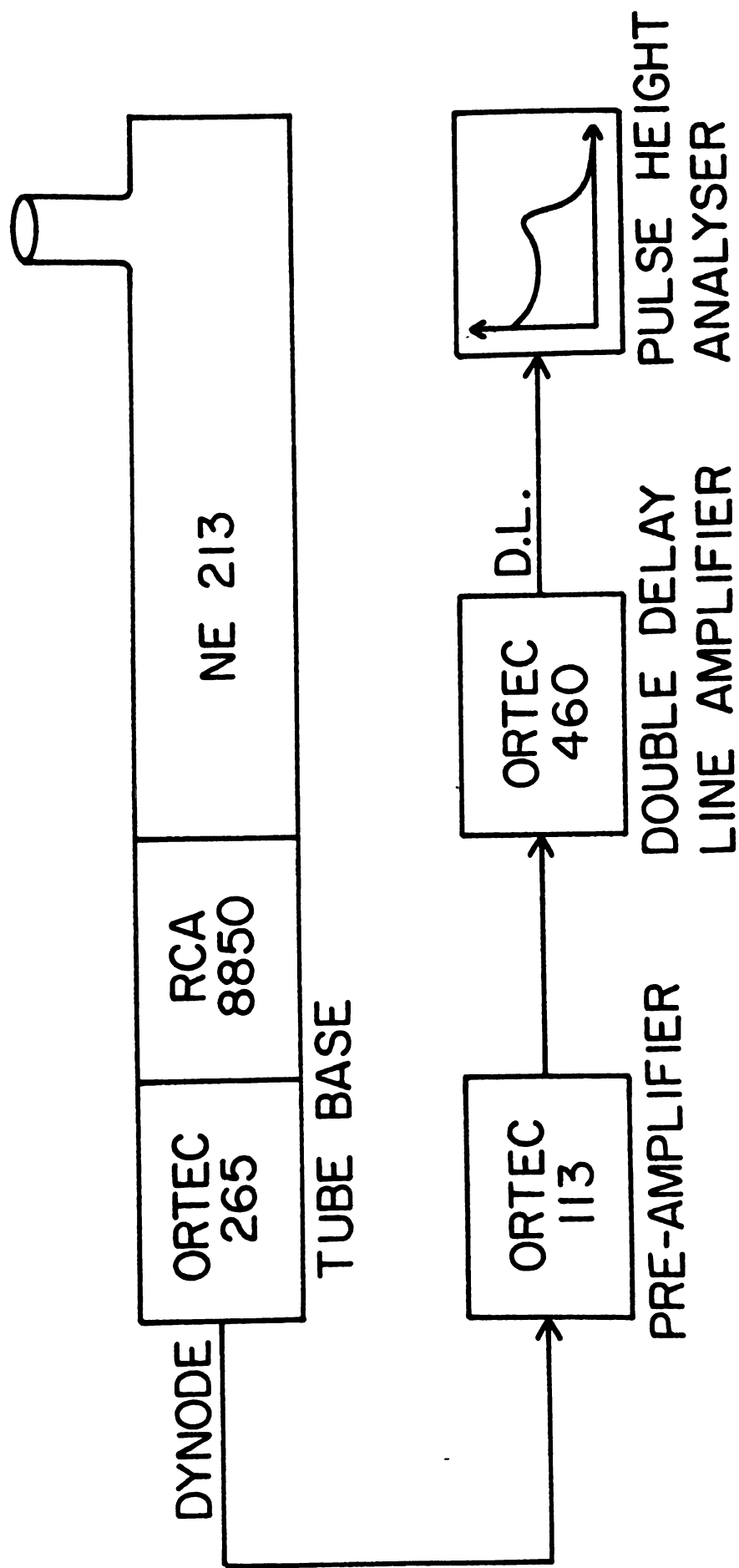


Figure E6. Block diagram of the electronics for measurements of the "wavelength-averaged attenuation length".

The resulting plot of intensity versus position reflects not only the attenuation in the liquid scintillator, but also attenuation due to scattering at the liquid/glass interface and absorption within the glass. We wish to know the attenuation in the liquid scintillator alone. By reducing the diameter of the cell, the path traveled through the liquid stays the same, but the number of reflections is increased. Therefore, by the following analysis we can determine the attenuation length of the liquid scintillator:

The transmission within the scintillator itself may be written as

$$(2) \quad I/I_0 = \exp\left(\frac{-d}{\lambda_\ell}\right)$$

where λ_ℓ is the attenuation length in the liquid scintillator. Then the transmission of light down the cell, including losses at reflection, is

$$(3) \quad I/I_0 = \exp\left(\frac{-d}{\lambda_\ell}\right) R^n,$$

where n is the number of reflections and R is the fraction of the light reflected at each reflection. For a ray traveling at a given angle θ from the z axis of the cylinder

$$(4) \quad d = \frac{z}{\cos\theta}$$

$$(5) \quad n = \left[\frac{z \tan\theta}{D} \right]$$

where D is the diameter of the tube and $[x]$ is the greatest-integer function. For n large the approximation of equation 5 by

$$(6) \quad n = \frac{z \tan\theta}{D}$$

is sufficient. Then using equations 4 and 6, R^n can be expressed as

$$(7) \quad R^n = \exp\left(\frac{-Cd \sin\theta}{D}\right),$$

where $C = -\ln R$. By letting

$$(8) \quad \lambda_g = \frac{D}{C \sin\theta}$$

equation 3 can be written in the more tractable form

$$(9) \quad I/I_0 = \exp\left(-\frac{d}{\lambda_\ell} - \frac{d}{\lambda_g}\right)$$

where λ_g represents losses other than those in the liquid, e.g., losses in the glass. We can define a total attenuation length λ by

$$(10) \quad \frac{1}{\lambda} = \left(\frac{1}{\lambda_\ell} + \frac{1}{\lambda_g}\right).$$

For different diameters (D_1, D_2) of cells, equation 8 gives the relation

$$(11) \quad \lambda_g(D_1) = \frac{D_1 \lambda_g(D_2)}{D_2}.$$

Of course, λ_ℓ is the same in each cell. Then using equations 10 and 11 to eliminate λ_g we finally obtain for λ_ℓ :

$$(12) \quad \lambda_\ell = \frac{\lambda(D_2) \left(\frac{D_2}{D_1} - 1\right)}{\frac{D_2}{D_1} - \frac{\lambda(D_2)}{\lambda(D_1)}},$$

where $\lambda(D_2)$ and $\lambda(D_1)$ are the total attenuation lengths for cells of the two diameters, D_2 and D_1 .

A 22 mm O.D. cell, otherwise comparable to the 45 mm O.D. cell (Fig. E1), was used to collect data following the same procedure as for the 45 mm O.D. cell. The data for both cells are shown in Fig. E7.

Figure E7. Compton edge channel vs. path length for NE213 in the unpainted 45 mm and 22 mm cell (darkened line indicated region over which the least squared fit was performed).

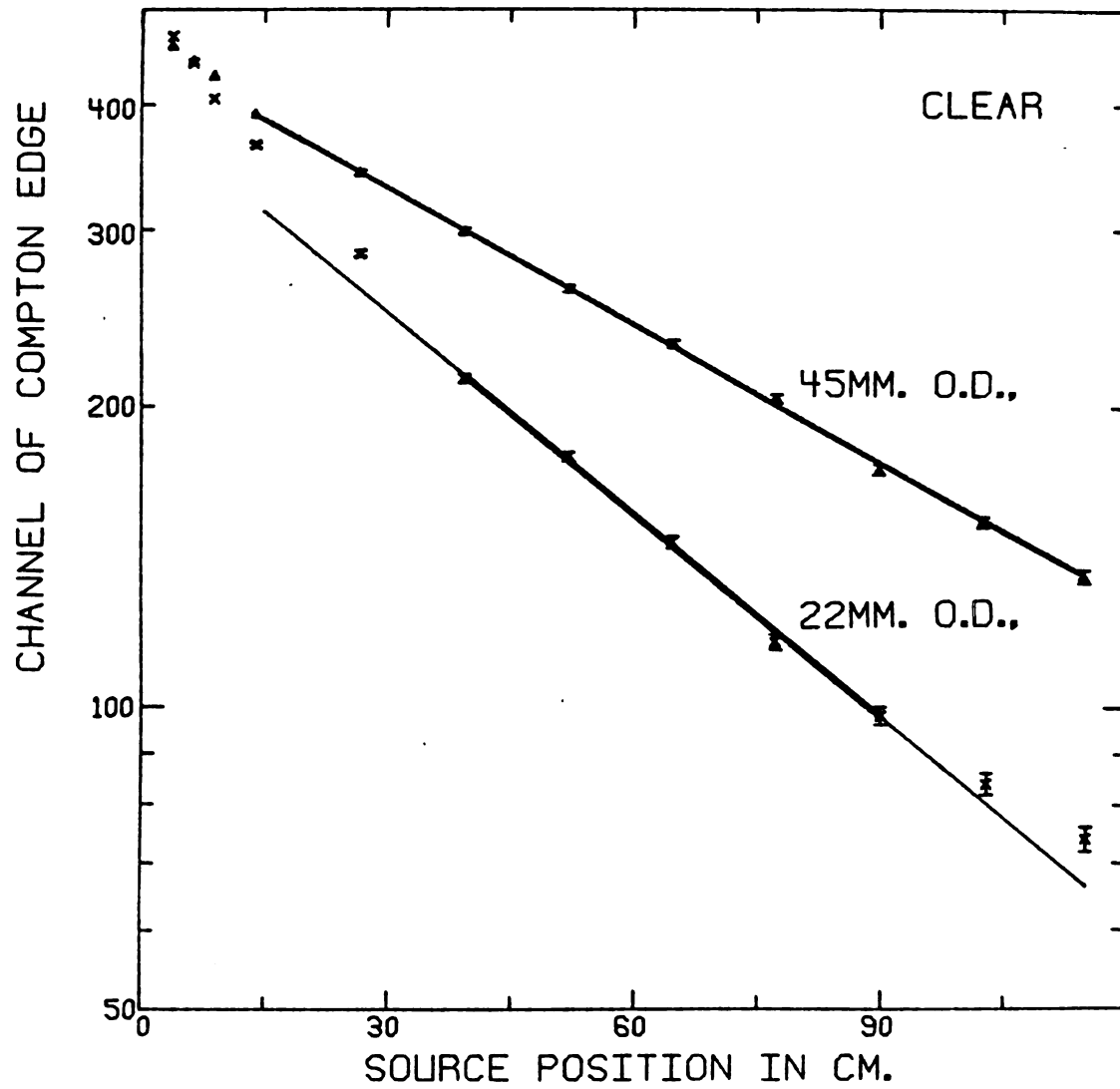


Figure E7.

Applying a least-squares fit to the data in Fig. E7 gives us the total attenuation lengths $\lambda(D_1)$ and $\lambda(D_2)$ as listed in Table E2. These are measured with respect to the z axis. However, not all of the light travels parallel to the z axis. Averaging the path length over the solid angle for which there is total internal reflection and allowing for exponential attenuation of the light gives the expression for the mean path length:

$$(13) \quad d = \frac{\int_0^{2\pi} \int_0^{\frac{\pi}{2} - \theta_c} d \exp(-d/\lambda) \sin\theta d\theta d\phi}{\int_0^{2\pi} \int_0^{\frac{\pi}{2} - \theta_c} \exp(-d/\lambda) \sin\theta d\theta d\phi},$$

where θ_c is the critical angle. Substituting for d from equation 4 and integrating over ϕ yields

$$(14) \quad \langle d \rangle = \frac{z \int_0^{\frac{\pi}{2} - \theta_c} \tan\theta \exp\left(-\frac{z}{\lambda \cos\theta}\right) d\theta}{\int_0^{\frac{\pi}{2} - \theta_c} \sin\theta \exp\left(-\frac{z}{\lambda \cos\theta}\right) d\theta}$$

A corrected attenuation length, λ (corrected), can be defined by the expression:

$$(15) \quad \exp\left(-\frac{z}{\lambda}\right) = \exp\left(\frac{\langle d \rangle}{\lambda \text{ (corrected)}}\right),$$

$$(16) \quad \text{that is, } \lambda \text{ (corrected)} = \frac{\langle d \rangle}{z} \lambda.$$

λ (corrected) is now the appropriate attenuation length for expressions 12 and 14. However, since the expression for $\langle d \rangle/z$ requires λ (corrected) we must use the uncorrected value of attenuation length as a first approximation and iterate until the function converges. The expression for $\langle d \rangle/z$ does not depend strongly on the value of $\langle z \rangle$, so a

Table II. Wavelength-averaged attenuation length in meters for unpainted cells containing NE 213.

D (mm)	λ (D)	λ (corrected)	λ_g
45 O.D.	0.954 ± 0.009	1.16 ± 0.01	2.53 ± 0.07
22 O.D.	0.645 ± 0.015	0.78 ± 0.02	1.23 ± 0.09

λ_g : 2.16 0.24

typical value of z for the measurements taken was used. The integration was done numerically on an XDS Sigma-7 computer, as was the iteration.

The critical angle θ_c was obtained by measuring the index of refraction of the liquid scintillator using a prism spectrometer and fitting the data to the equation²⁵

$$(17) \quad n^2 = 1 + \frac{A}{(\omega_0^2 - \omega^2)} ,$$

where n is the index of refraction, ω is the frequency of the light, and A and ω_0 are constants. The index of refraction was measured over the range of 4047 Å through 5791 Å. At 4250 Å the index of refraction 1.52792 ± 0.00021 , which in turn gives a critical angle of $40.881^\circ \pm 0.007^\circ$.

With this value of θ_c , $\langle d \rangle / z$ was found to be 1.214 ± 0.001 . Multiplying this value by 0.954 ± 0.009 m (from Table E2) for (D) of the 45 mm cell gives us a λ (corrected) of $1.16 \pm .01$ m. Similarly, for the 22 mm cell the λ (D) value of 0.645 ± 0.015 m gives us a λ (corrected) of 0.78 ± 0.02 m. Substituting these values of λ (corrected) into equation 12 gives us an attenuation length in the liquid of 2.16 ± 0.24 m.

The cells were then painted black to eliminate total internal reflection. It was thought that the only attenuation would be that in the liquid plus a $1/R^2$ attenuation which could be easily corrected for. It turns out, however, that there is still total internal reflection, now at the liquid/glass interface. Since the critical angle is much larger than at the glass/air interface, the number of reflections

Table III. Practical attenuation lengths in meters for blackpainted cells containing NE 213.

D (mm)	λ (D)	λ (corrected)	λ_g
45 O.D.	1.82 ± 0.16	1.85 ± 0.16	4.81 ± 0.12
22 O.D.	1.26 ± 0.08	1.28 ± 0.08	2.23 ± 0.12
$\lambda_g: 3.00 \pm 0.94$			

is reduced, and attenuation at the interface contributes less. However, the solid angle of light detected is so much smaller that the Compton edge is smeared out. The smearing of the Compton edge makes it difficult to obtain accurate values for the attenuation.

The critical angle was determined by measuring the critical angles for the various lines ($6764 \text{ \AA} - 4689 \text{ \AA}$) of the krypton laser and the 4416 \AA line of the he-cd laser. The index of refraction of the glass was found by using the fitted equation for the index of refraction of the NE 213 and measuring the relative index of refraction of the NE 213 to glass. The data for the index of refraction of the glass were then fitted to equation 17. The resulting relative index of refraction for NE 213 to glass was 1.0307 ± 0.0002 , giving a critical angle of $75.98^\circ \pm 0.04^\circ$.

With this value of θ_c , $\langle d \rangle / z$ was found to be 1.015 ± 0.001 .

The data for the blackened cells were taken in the same manner as for the clear cells. The data are shown in Fig. E8. The attenuation lengths were computed as before, with the exception that the appropriate diameters are the inside diameters, 41 and 19 mm. The results for the blackened cells, which are listed in Table E3, give $\lambda_\ell = 3.00 \pm 0.94 \text{ m}$.

Figure E8. Compton edge channel vs. path length for NE213 in the black painted 45 mm and 22 mm cells (darkened line indicated region over which the least-squares fit was performed).

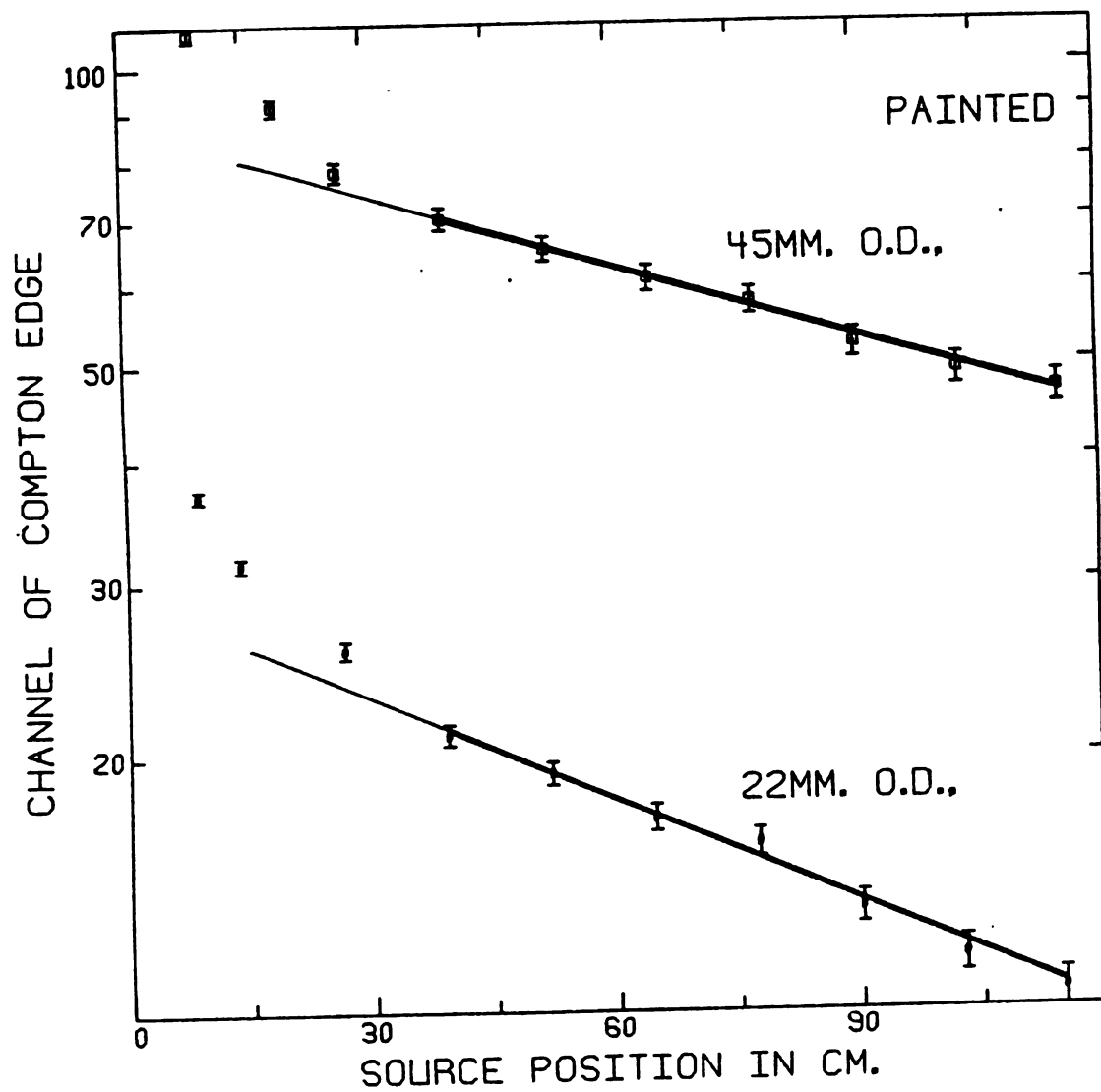


Figure E8.

E3. CONCLUSIONS

The values of 1.85, 3.02, and 1.22, 1.40 meters for the attenuation length of 4416 Å and 4689 Å light in NE 213 and NE 224, respectively, show that NE 213 has the advantage of having a longer attenuation length than NE 224. Also, both scintillators show more absorption at the shorter wavelength.

The attenuation lengths measured by the laser method are precise, but the wavelength-averaged attenuation lengths are more appropriate for actual design applications. Due to poor Compton-edge resolution, the value of the attenuation length in NE 213 obtained with the painted cells, 3.00 ± 0.94 m, may be suspect, although it is not inconsistent with $\lambda = 2.16 \pm 0.24$ meters obtained by not painting the cells. The latter value is then what we believe accurately represents the practical attenuation length in NE 213. A 46% end-to-end attenuation measured in a detector containing NE 224 at Michigan State University implies a value of 1.36 meters for the attenuation length.²⁶ It should be noted, however, that these values include attenuation in the walls of the detector itself, whereas the values in Table I do not. Kuijper, Tiesinga, and Jonker²⁷ by using a similar method, obtained an attenuation length of 1.5 meters measured over the first 10 cm of travel. This is,

of course, where the most rapid attenuation occurs for reasons stated earlier. For large detectors our value for the attenuation length may be more appropriate, since it was measured over a 1.24-meter path.

In designing a detector it is clear that the shape of the vessel is of importance. The 22 mm O.D. cell had a higher rate of attenuation than the 45 mm O.D. cell due to the greater number of reflections per unit length traveled. Complex geometries may pose problems for that reason. Evers et al.²⁸ report an attenuation of a factor of four over the full length of an 80 mm x 1 m glass cell filled with NE 213. This implies an attenuation length of 0.72 meters. This is not consistent with the increasing attenuation length versus cell diameter we observed. However, the condition of the surface of their cell may differ from ours and the composition of the glass is unknown to us and may account for the shorter-than-expected attenuation length for a large-diameter cell.

Much of the light lost at each reflection is thought to be due to scattering, since the attenuation length of 4250 Å light in Pyrex²⁹ is large compared to the actual attenuation observed. The glass used in our cells was extruded and left with its original surface. The annealing process may allow further imperfections to form on the surface. By polishing the glass, better light transmission might be achieved. Also, perhaps there may be better material than glass for this application.

LIST OF REFERENCES

LIST OF REFERENCES

1. Manufactured by Nuclear Enterprises, Inc., San Carlos, CA 94070, USA.
2. Donald L. Horrocks, Application of Liquid Scintillation Counting, New York: Academic Press, 1974, p. 35.
3. Donald L. Horrocks, J. Chem. Phys. 52, 1567 (1970).
4. Donald L. Horrocks, Application of Liquid Scintillation Counting, New York: Academic Press, 1972, p. 45.
5. V.A. Doolin, and V.M. Litjaev, Nucl. Instr. and Meth. 82, 179 (1970).
6. Ortec Catalog 1002, Ortec Incorporated, 100 Midland Road, Oak Ridge, TN 37830, USA, p. 70.
7. Doolin and Litjaev, 178.
8. Ibid.
9. R.F. Post and L.I. Schiff, Phys. Rev. 80, 1113 (1950).
10. F.T. Kuchnir and F.J. Lynch, IEEE Trans. Nucl. Sci. NS-15, no. 3. (June 1969).
11. R.A. Winyard and G.W. McBeth, Nucl. Inst. and Meth. 98, 525 (1972).
12. Ibid.
13. B. Sabbah and A. Suhami, Nucl. Instr. and Meth. 98, 104 (1968).
14. Ortec Model 460 Delay Line Amplifier Manual, p. 10.
15. Manufactured by Nuclear Enterprises, Inc.
16. Manufactured by RCA, Harrison, NJ
17. G.G. Kelley, P.R. Bell, K.C. Davis, and H.J. Lazar, I.R.E. Trans. Nucl. Sci. NS-3, 56 (1956).
18. Kuchnir and Lynch, 108.

19. E.C. Hagen and P.C. Eklund, Rev. Sci. Instr. 47, no. 9, 1144 (Sept. 1976).
20. R.A. Winyard, J.E. Lutkin and G.W. McBeth, Nucl. Instr. and Meth. 95, 143 (1971).
21. Manufactured by Amperex Electronic Corporation, Hicksville, Long Island, NY 11802, USA.
22. Handbook of Chemistry and Physics, Chemical Rubber Co., 54th ed.
23. Manufactured by Nuclear Enterprises, Inc., San Carlos, CA 94070, USA.
24. Obtained from Nuclear Enterprises, Inc.
25. E. Hecht and A. Zajac, Optics (Addison-Wesley, 1974) p. 40.
26. Ranjan K. Bhowmik, Robert R. Doering, Lawrence E. Young, Sam M. Austin, Aaron Galonsky and Steve D. Schery, Nucl. Instr. and Meth. 143 (1977) 63.
27. P. Kuijper, C.J. Tiesinga, and C.C. Jonker, Nucl. Instr. and Meth. 42 (1966) 56.
28. D. Evers, E. Spindler, P. Konrad, K. Rudolf, W. Assmann, and P. Speer, Nucl. Instr. and Meth. 124 (1975) 24.
29. G.W.C. Kaye and T.H. Laby, Tables of Physical and Chemical Constants, (John Wiley & Sons, Inc., 1966) p. 86.